

Planck intermediate results. XXI. Comparison of polarized thermal emission from Galactic dust at 353 GHz with optical interstellar polarization

Planck Collaboration: P. A. R. Ade⁷⁸, N. Aghanim⁵⁴, D. Alina^{83,10}, G. Aniano⁵⁴, C. Armitage-Caplan⁸¹, M. Arnaud⁶⁷, M. Ashdown^{64,6}, F. Atrio-Barandela¹⁸, J. Aumont⁵⁴, C. Baccigalupi⁷⁷, A. J. Banday^{83,10}, R. B. Barreiro⁶¹, E. Battaner⁸⁵, C. Beichman¹¹, K. Benabed^{55,82}, A. Benoit-Lévy^{24,55,82}, J.-P. Bernard^{83,10}, M. Bersanelli^{33,47}, P. Bielewicz^{83,10,77}, J. J. Bock^{62,11}, J. R. Bond⁹, J. Borrill^{13,79}, F. R. Bouchet^{55,82}, F. Boulanger⁵⁴, C. Burigana^{46,31}, J.-F. Cardoso^{68,1,55}, A. Catalano^{69,66}, A. Chamballu^{67,15,54}, R.-R. Chary⁵³, H. C. Chiang^{27,7}, P. R. Christensen^{74,36}, S. Colombi^{55,82}, L. P. L. Colombo^{23,62}, C. Combet⁶⁹, F. Couchot⁶⁵, A. Coulais⁶⁶, B. P. Crill^{62,75}, A. Curto^{6,61}, F. Cuttaia⁴⁶, L. Danese⁷⁷, R. D. Davies⁶³, R. J. Davis⁶³, P. de Bernardis³², A. de Rosa⁴⁶, G. de Zotti^{43,77}, J. Delabrouille¹, F.-X. Désert⁵¹, C. Dickinson⁶³, J. M. Diego⁶¹, S. Donzelli⁴⁷, O. Doré^{62,11}, M. Douspis⁵⁴, J. Dunkley⁸¹, X. Dupac³⁹, T. A. Enßlin⁷², H. K. Eriksen⁵⁸, E. Falgarone⁶⁶, L. Fanciullo⁵⁴, F. Finelli^{46,48}, O. Forni^{83,10}, M. Frailis⁴⁵, A. A. Fraisse²⁷, E. Franceschi⁴⁶, S. Galeotta⁴⁵, K. Ganga¹, T. Ghosh⁵⁴, M. Giard^{83,10}, Y. Giraud-Héraud¹, J. González-Nuevo^{61,77}, K. M. Górski^{62,86}, A. Gregorio^{34,45,50}, A. Gruppuso⁴⁶, V. Guillet⁵⁴ *, F. K. Hansen⁵⁸, D. L. Harrison^{57,64}, G. Helou¹¹, C. Hernández-Monteagudo^{12,72}, S. R. Hildebrandt¹¹, E. Hivon^{55,82}, M. Hobson⁶, W. A. Holmes⁶², A. Hornstrup¹⁶, K. M. Huffenberger²⁵, A. H. Jaffe⁵², T. R. Jaffe^{83,10}, W. C. Jones²⁷, M. Juvela²⁶, E. Keihänen²⁶, R. Kesitalo^{22,13}, T. S. Kisner⁷¹, R. Kneissl^{38,8}, J. Knoche⁷², M. Kunz^{17,54,3}, H. Kurki-Suonio^{26,41}, G. Lagache⁵⁴, A. Lähteenmäki^{2,41}, J.-M. Lamarre⁶⁶, A. Lasenby^{6,64}, C. R. Lawrence⁶², R. Leonardi³⁹, F. Levrier⁶⁶, M. Liguori³⁰, P. B. Lilje⁵⁸, M. Linden-Vørnle¹⁶, M. López-Cañiego⁶¹, P. M. Lubin²⁸, J. F. Macías-Pérez⁶⁹, B. Maffei⁶³, A. M. Magalhães⁶⁰, D. Maino^{33,47}, N. Mandolesi^{46,5,31}, M. Maris⁴⁵, D. J. Marshall⁶⁷, P. G. Martin⁹, E. Martínez-González⁶¹, S. Masi³², S. Matarrese³⁰, P. Mazzotta³⁵, A. Melchiorri^{32,49}, L. Mendes³⁹, A. Mennella^{33,47}, M. Migliaccio^{57,64}, M.-A. Miville-Deschênes^{54,9}, A. Moneti⁵⁵, L. Montier^{83,10}, G. Morgante⁴⁶, D. Mortlock⁵², D. Munshi⁷⁸, J. A. Murphy⁷³, P. Naselsky^{74,36}, F. Nati³², P. Natoli^{31,4,46}, C. B. Netterfield²⁰, F. Novello⁶³, D. Novikov⁵², I. Novikov⁷⁴, C. A. Oxborrow¹⁶, L. Pagano^{32,49}, F. Pajot⁵⁴, R. Paladini⁵³, D. Paoletti^{46,48}, F. Pasian⁴⁵, O. Perdereau⁶⁵, L. Perotto⁶⁹, F. Perrotta⁷⁷, F. Piacentini³², M. Piat¹, D. Pietrobon⁶², S. Plaszczynski⁶⁵, F. Poidevin²⁴, E. Pointecouteau^{83,10}, G. Polenta^{4,44}, L. Popa⁵⁶, G. W. Pratt⁶⁷, S. Prunet^{55,82}, J.-L. Puget⁵⁴, J. P. Rachen^{21,72}, W. T. Reach⁸⁴, R. Rebolo^{59,14,37}, M. Reinecke⁷², M. Remazeilles^{63,54,1}, C. Renault⁶⁹, S. Ricciardi⁴⁶, T. Riller⁷², I. Ristorcelli^{83,10}, G. Rocha^{62,11}, C. Rosset¹, G. Roudier^{1,66,62}, B. Rusholme⁵³, M. Sandri⁴⁶, G. Savini⁷⁶, L. D. Spencer⁷⁸, V. Stolyarov^{6,64,80}, R. Stompor¹, R. Sudiwala⁷⁸, D. Sutton^{57,64}, A.-S. Suur-Uski^{26,41}, J.-F. Sygnet⁵⁵, J. A. Tauber⁴⁰, L. Terenzi⁴⁶, L. Toffolatti^{19,61}, M. Tomasi⁴⁷, M. Tristram⁶⁵, M. Tucci^{17,65}, G. Umata⁴², L. Valenziano⁴⁶, J. Valiviita^{41,26,58}, B. Van Tent⁷⁰, P. Vielva⁶¹, F. Villa⁴⁶, L. A. Wade⁶², B. D. Wandelt^{55,82,29}, and A. Zonca²⁸

(Affiliations can be found after the references)

Received XX April 2014; accepted XX 2014

ABSTRACT

The *Planck* survey provides unprecedented full-sky coverage of the submillimetre polarized emission from Galactic dust. In addition to the information on the direction of the Galactic magnetic field, this also brings new constraints on the properties of dust. The dust grains that emit the radiation seen by *Planck* in the submillimetre also extinguish and polarize starlight in the optical. Comparison of the polarization of the emission and of the interstellar polarization on selected lines of sight probed by stars provides unique new diagnostics of the emission and light scattering properties of dust, and therefore ultimately of the important model parameters, composition, size, shape, and alignment. Using ancillary catalogues of interstellar polarization and extinction of starlight, we obtain the degree of polarization, p_V , and the optical depth in the V band to the star, τ_V . We extract the submillimetre polarized intensity, P_S , and total intensity, I_S , measured toward these stars in the *Planck* 353 GHz channel. We compare the polarization direction (position angle) measured in the optical with that measured at 353 GHz, and compare the column density measure $E(B - V)$ with that inferred from the *Planck* product map of the submillimetre dust optical depth. For those lines of sight with little CO integrated intensity, as well as having polarization directions close to orthogonal and comparable values of the estimated column density, we correlate the projected polarization efficiencies in emission, Q_S/I_S and U_S/I_S , with those in extinction, q_V/τ_V and u_V/τ_V , to measure the polarization ratio $R_{S/V} = (P_S/I_S)/(p_V/\tau_V)$. We find a polarization ratio $R_{S/V} = 4.3$ with statistical and systematic uncertainties 0.2 and 0.4, respectively. We focus directly on the polarization properties of the aligned grain population alone via an alternative ratio, the relative efficiency $R_{p/p} = P_S/p_V = 5.6 \text{ MJy sr}^{-1}$, with statistical and systematic uncertainties 0.2 and 0.4 MJy sr⁻¹, respectively. Our estimate of $R_{S/V}$ is reasonably compatible with predictions based on a range of current dust models that have been developed for the diffuse interstellar medium, not yet very discriminating among them. However, the observed $R_{p/p}$ is a more discriminating diagnostic for the polarizing grain population and is not compatible with predictions, the observations being higher by a factor of about 2.5. These new diagnostics from *Planck*, including the spectral dependence in the submillimetre, will be important for constraining and understanding the full complexity of the grain models, and for further interpretation of the *Planck* thermal dust polarization and refining the separation of this contamination of the cosmic microwave background.

Key words. ISM: general – ISM: dust, extinction, polarization – Submillimetre: ISM

1. Introduction

*Planck*¹ has the capability of measuring the linear polarization of the cosmic microwave background (CMB), a valuable probe

¹ *Planck* (<http://www.esa.int/Planck>) is a project of the European Space Agency (ESA) with instruments provided by two sci-

* Corresponding author: V. Guillet, Vincent.Guillet@ias.u-psud.fr

for precision cosmology (Planck Collaboration I 2014; Planck Collaboration XVI 2014). One of the diffuse foregrounds contaminating the CMB signal is thermal emission by diffuse interstellar dust. Because interstellar polarization of starlight is commonly seen in the optical, from differential extinction by aspherical dust particles that are aligned with respect to the Galactic magnetic field (Hall 1949; Hiltner 1949; Davis & Greenstein 1951), it was predicted that the thermal emission from these grains would be polarized (Stein 1966) and indeed this is the case (Hildebrand et al. 1999; Benoît et al. 2004; Planck Collaboration Int. XIX 2014 and references therein).

The CMB fades toward higher frequencies, whereas the thermal dust emission increases, and so dust becomes the dominant signal in the submillimetre (Planck Collaboration XII 2014). The HFI instrument (Lamarre et al. 2010) on *Planck* has multifrequency polarization sensitivity in the “dust channels” covering the spectral range where this transition occurs, up to 353 GHz (Ade et al. 2010; Planck Collaboration I 2014). Understanding both the frequency dependence and spatial fluctuations of the polarized intensity from thermal dust will be important in refining the separation of this contamination of the CMB. With its sensitive all-sky coverage, *Planck* is providing the most comprehensive empirical data for this analysis (Planck Collaboration Int. XIX 2014; Planck Collaboration Int. XX 2014; Planck Collaboration Int. XXII 2014).

Planck observations of the submillimetre polarized sky also represent a great step forward for Galactic science. Aspects of dust polarization related to the Galactic magnetic field are explored in two *Planck* papers (Planck Collaboration Int. XIX 2014; Planck Collaboration Int. XX 2014). Planck Collaboration Int. XXII (2014) describes the spectral dependence of dust polarized emission in the diffuse ISM. The present article complements this work by deriving the normalization of the diffuse dust polarization SED to starlight polarization measured in the optical. This provides valuable new constraints on grain models.

Interstellar polarization of starlight by dust along the line of sight has been studied extensively during the last 60 years, from the ultra-violet to the infrared. The ratio of the polarization fraction to extinction, p/τ or polarization efficiency, is different from star to star, because of variations in the orientation of the magnetic field and in the dust asphericity and alignment efficiency along the line of sight. The spectral dependence of the degree of polarization (or polarization fraction), the polarization curve $p(\nu)$, has a peak in the optical (parameterized using a wavelength λ_{max} that is typically $0.55 \mu\text{m}$) and falls off toward both the infrared and the UV (Serkowski et al. 1975; Martin et al. 1992, 1999); by contrast, the extinction curve $\tau(\nu)$ increases with frequency from the infrared to the UV. The ratio of these, $p(\nu)/\tau(\nu)$, increases with decreasing frequency. The maximum observed values, which arise from optimal conditions of magnetic field orientation and dust alignment, range from a few tenths of percent in the far UV, to around 3 % in the V band, and up to 7 % in the K band (Martin et al. 1999).

Various models have been developed to reproduce the polarization and extinction spectral dependences with a combination of aligned and unaligned grains (e.g., Lee & Draine 1985; Li & Greenberg 1997; Voshchinnikov 2012). The most recent are further constrained by fitting the (pre-*Planck*) spectral energy distribution of dust emission in the infrared and submillimetre

(Draine & Fraisse 2009; Compiegne et al. 2011; Siebenmorgen et al. 2013). Efforts have also been made to predict the polarized emission quantitatively (Martin 2007; Draine & Fraisse 2009; Draine & Hensley 2013). In these models, silicate grains are taken to be aligned, as motivated by the observed polarization of the interstellar mid-infrared silicate absorption band (see e.g., Lee & Draine 1985 and references therein). Up to now there has been no clear observational evidence to distinguish whether carbon grains are aligned or not (but see Chiar et al. 2006) and so current models attempt fits to the data using both alignment alternatives for carbon grains, whether graphite or amorphous carbon. The new observational constraints from this paper bear on this question of the alignment of carbon grains.

By providing full-sky statistics on Galactic dust emission, both in total intensity and polarized intensity, *Planck* observations are forcing reconsideration of current dust models. Particularly challenging is the finding by Planck Collaboration Int. XXV (2014), following the work by Planck Collaboration XI (2014) and Planck Collaboration Int. XVII (2014), that the Draine & Li (2007) model tends to underpredict the amount of dust emission per unit extinction by a factor 1.9. Furthermore, the analysis by Planck Collaboration Int. XXV (2014) confirms the conclusion by Planck Collaboration XXIV (2011) and Planck Collaboration XI (2014) that the observed variations of dust temperature in the diffuse ISM cannot be understood without invoking significant variations in the intrinsic dust optical properties. For dust models applicable to the diffuse ISM this possibility has usually been ignored, but there has been some recent work in that direction (Cecchi-Pestellini et al. 2010; Jones et al. 2013).

Regarding polarization, Planck Collaboration Int. XXII (2014) finds that in the diffuse ISM the mean polarized intensity decreases faster with decreasing frequency than the total intensity. The present paper aims at completing this new picture of diffuse² dust by exploiting the *Planck* polarization data to determine the ratio of the polarization in the submillimetre to that in the optical along the same line of sight to a star, over many lines of sight. Just as in the aforementioned *Planck* papers that concerned intensity and extinction, our conclusions from polarization severely challenge current dust models.

This paper is organized as follows. In Sect. 2 we introduce the emission to extinction ratios in polarization that are analyzed in this paper and describe their diagnostic importance for dust modelling. The observational data with error estimates that are available in the submillimetre from the *Planck* maps are presented in Sect. 3, supplemented by Appendix A. Section 4, supplemented by Appendix B, describes the optical data from catalogues for many lines of sight to stars. The criteria for selecting suitable lines of sight are given in Sect. 5. The methodology for evaluation of the polarization ratios and the results for the diffuse ISM follow in Sect. 6 and the robustness of the results is discussed in Sect. 7. In the discussion (Sect. 8) we explore how these results from polarization provide new constraints on dust models. We conclude with a short summary in Sect. 9.

² In the Galactic plane and in dense molecular clouds, even when optical polarization data are available, the interpretation of the optical and submillimetre polarization is complicated by many issues: beam dilution; distortions in the magnetic field topology; changes in the degree of alignment along the line of sight; grain evolution; and ranges of grain temperature and optical depth that affect which grains dominate the polarized emission in various parts of the submillimetre spectrum. Such complex regions are not considered here. We limit our analysis to lines of sight through the diffuse ISM, for which more homogeneous properties might be expected.

entific consortia funded by ESA member states (in particular the lead countries France and Italy), with contributions from NASA (USA) and telescope reflectors provided by a collaboration between ESA and a scientific consortium led and funded by Denmark.

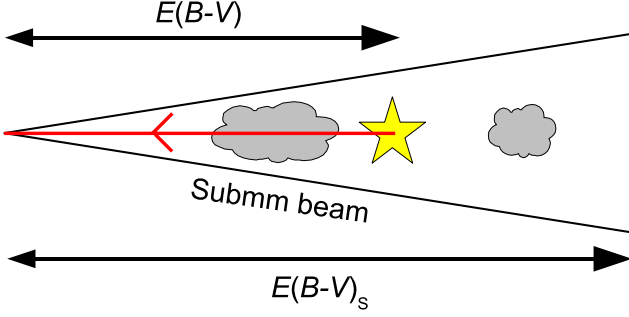


Fig. 1. Instrumental-beam and line-of-sight components affecting the comparison of polarized emission with interstellar polarization from differential extinction of a star. $E(B - V)$ is the colour excess to the star, while $E(B - V)_s$ is the submillimetre optical depth converted to a colour excess (Sect. 3.3).

2. Diagnostic polarization ratios involving dust emission and extinction

In this paper we evaluate the ratio of the polarization at 353 GHz in the submillimetre, where the signal-to-noise ratio (S/N) is highest for dust polarized emission, to the optical interstellar polarization in the V band, near the peak of the polarization curve. A first condition necessary for this comparison to be meaningful is met: interstellar polarization (differential extinction) in the V band is dominated by the dust grains that emit thermal radiation at 353 GHz, the so-called “large” grains (around $0.1 \mu\text{m}$ in size, e.g., Draine & Li 2007). Various factors, like column density, grain shape and asphericity (elongation/flattening), grain alignment efficiency, and magnetic field orientation, affect polarization in the submillimetre and in the optical in similar ways (Martin 2007). The ratio of submillimetre to optical polarization is therefore expected to be a robust diagnostic, characterizing the dust optical properties alone and providing a valuable new quantitative probe with which to constrain complex dust models.

As data we have the optical depth to the star in the V band, τ_V , and the degree of polarization of the transmitted starlight, p_V (see Sect. 3), together with the total submillimetre emission, I_s , and the polarized emission, P_s for the same line of sight (see Sect. 4). A typical geometry is shown schematically in Fig. 1. In the optical, interstellar polarization and extinction arise from dust averaged over the angular diameter of the star, which is tiny compared to the *Planck* beam. Furthermore, these optical observations probe the ISM only up to the distance of the star, while submillimetre observations probe the whole line of sight through the Galaxy, thus including a contribution from any background ISM (see Fig. 1). As will be discussed below, the effects of these differences can be mitigated and assessed.

These geometrical considerations motivate examination of the ratio

$$R_{S/V} = \frac{P_s/I_s}{p_V/\tau_V}, \quad (1)$$

a non-dimensional quantity where both numerator and denominator are themselves non-dimensional ratios that apply to the same geometry (common beam and common portion of the line of sight). Furthermore, by virtue of the normalization both P_s/I_s and p_V/τ_V , the submillimetre and optical polarization efficiencies, do not depend on the column density and become less sensitive to various factors like the size distribution, grain heating, and opacity that affect the numerator and denominator in similar

ways. For all of these reasons, $R_{S/V}$ should be a robust diagnostic (Martin 2007).

As discussed in Sect. 1, current models of interstellar dust commonly feature multiple grain components and not all components (even those that are in thermal equilibrium with the interstellar radiation field and are the major contributors to optical extinction and submillimetre emission) might be aspherical and aligned. Both I_s and τ_V entail the full complexity from the contributions of aligned and non-aligned grain populations and so introduce this complexity into $R_{S/V}$, although these effects compensate at least partially because they enter only through I_s/τ_V (Martin 2007). On the other hand, the polarized emission, P_s , and the degree of polarization toward the star, p_V , isolate properties of the polarizing grains alone. In particular, their ratio

$$R_{P/p} = P_s/p_V \quad (2)$$

addresses how efficient the polarizing grains are in producing polarized submillimetre emission compared to optical interstellar polarization. This relative efficiency $R_{P/p}$ has the units of polarized intensity, here MJy sr^{-1} . Although P_s and p_V both depend on column density, this ratio is more sensitive to the above geometrical effects and particular attention must be paid to avoid lines of sight with significant background emission. Through P_s , $R_{P/p}$ is directly dependent on the submillimetre emissivity of the polarizing grains and on the intensity of the interstellar radiation field. Nevertheless, $R_{P/p}$ can provide even stronger constraints on the aligned grains than $R_{S/V}$ can.

In summary, the diagnostic ratios $R_{S/V}$ and $R_{P/p}$ provide new internal (dust relative to dust) consistency checks for dust models. They relate the polarization properties of dust grains detected via submillimetre emission to the polarization properties of the same grains detected in optical extinction, isolating the dust properties (optical constants, size distributions, and, more subtly, shape) from other factors such as dust-to-gas ratio, column density, magnetic field structure, or overall dust alignment efficiency.

3. Observations of polarized thermal emission from dust

3.1. *Planck* Data

The *Planck* HFI 353 GHz polarization maps that we used for the Stokes parameters Q_s and U_s (Planck Collaboration Int. XIX 2014) were those from the full mission with five full-sky surveys. These have been generated in exactly the same manner as the data publicly released in March 2013 and described in Planck Collaboration I (2014) and associated papers (Planck Collaboration VI 2014; Planck Collaboration VII 2014; Planck Collaboration VIII 2014; Planck Collaboration IX 2014; Planck Collaboration X 2014).³ The analysis in Planck Collaboration XVI (2014) shows the very good consistency of cosmological models that have been derived from intensity only with polarization data at small scales (high CMB multipoles). However, as detailed in Planck Collaboration VI (2014) (see their Fig. 27), the 2013 polarization data are known to be affected by systematic effects at low multipoles which were not yet fully corrected, and thus these data were not used for cosmology.⁴ We have been

³ Note, however, that the publicly released data include only temperature (intensity) maps, based on the first two surveys.

⁴ The full mission maps for intensity as well as for polarization will be made publicly available in fall 2014.

careful to check that the Galactic science results in this paper are robust with respect to these systematics.⁵

Intercalibration uncertainties between HFI polarization sensitive bolometers and differences in bolometer spectral transmissions introduce a leakage from intensity I into polarization Q and U , the main source of systematic errors (Planck Collaboration VI 2014). On-sky measurements bolometer by bolometer in judiciously-chosen regions can be used to identify the leakage and so to deduce the effective bandpass mismatch coefficients that are needed to predict the amount of leakage from the dust emission intensity into polarization (Planck Collaboration IX 2014). The maps used in this first series of polarization papers were corrected for the leakage in this way (Planck Collaboration Int. XIX 2014; Planck Collaboration Int. XX 2014; Planck Collaboration Int. XXII 2014).

At 353 GHz the dispersion arising from CMB polarization anisotropies is much lower than the instrumental noise for Q_S and U_S (Planck Collaboration VI 2014) and so has a negligible impact on our analysis (see Sect. 7.2). The cosmic infrared background (CIB) was assumed to be unpolarized (Planck Collaboration Int. XIX 2014).

For the intensity of thermal emission from Galactic dust, I_S , we begin with the corresponding *Planck* HFI 353 GHz map I_{353} from the same five-survey internal release, corrected for the CMB dipole. From a Galactic standpoint, I_{353} contains small amounts of contamination from the CMB, the CIB (Planck Collaboration XXX 2014), and zodiacal dust emission (Planck Collaboration XIV 2014). Models for the CMB fluctuations (using SMICA; Planck Collaboration XII 2014) and zodiacal emission (Planck Collaboration XIV 2014) were removed. For this study of Galactic dust emission we subtract the derived zero offset from the map, which effectively removes the CIB monopole (Planck Collaboration VI 2014; Planck Collaboration VIII 2014; Planck Collaboration XI 2014). The level of the CIB fluctuations (the anisotropies), estimated by Planck Collaboration XI (2014) to be $0.016 \text{ MJy sr}^{-1}$, introduces this uncertainty in I_S .

To increase the S/N of the *Planck* HFI measurements on lines of sight to the target stars (Sect. 4), especially in the diffuse ISM, the Stokes parameters I_S , Q_S , and U_S , were smoothed with a Gaussian centred on the star, and the corresponding noise covariance matrix was calculated (see Appendix A of Planck Collaboration Int. XIX 2014 for details). The *Planck* HFI 353 GHz maps have a native resolution of $5'$ and a HEALPix⁶ (Gorski et al. 2005) grid pixelization corresponding to $N_{\text{side}} = 2048$. Smoothing the *Planck* data accentuates the beam difference relative to the stellar probe (Fig. 1). Therefore, there is a compromise between achieving higher S/N and maintaining high resolution. The original S/N, and thus any compromise, depends on the region being studied. However, for simplicity we adopted a common Gaussian smoothing kernel, with a full width at half maximum (FWHM) of $5'$ (the effective beam is then $7'$), and explored the robustness of our results using different choices (Sect. 7.2).

⁵ The systematic errors that we quote include uncertainties associated with residual systematics as estimated by repeating the analysis on different subsets of the data. We have also checked our data analysis on the latest version of the maps available to the consortium to verify that the results are consistent within the uncertainties quoted in this paper.

⁶ see <http://healpix.jpl.nasa.gov> and <http://healpix.sourceforge.net>

3.2. Position angle in polarized emission

The orientation of the plane of vibration of the electric vector of the polarized radiation is described by a position angle with respect to North, here in the Galactic coordinate system. North corresponds to positive Q . In HEALPix, the native coordinate system of *Planck*, the position angle increases to the West, whereas in the IAU convention the position angle increases to the East; this implies opposite sign conventions for U (Planck Collaboration Int. XIX 2014). In this paper, all position angles, whether ψ_S in the submillimetre or ψ_V in the optical, are given in the IAU coordinate system to follow the use in the ISM literature.

On the other hand, all Stokes parameters, whether *Planck* Q_S , U_S in the submillimetre or q_V , u_V derived in the optical, are in the HEALPix convention. This accounts for the minus sign both in Eq. 3 and in its inverse form, Eq. 4 below.

Thus from the *Planck* data we find

$$\psi_S = \frac{1}{2} \arctan(-U_S, Q_S) \in [-90^\circ, 90^\circ]. \quad (3)$$

To recover the correct full range of position angles (either $[0^\circ, 180^\circ]$, or $[-90^\circ, 90^\circ]$ as used for ψ_S here) attention must be paid to the signs of both U_S and Q_S , not just of their ratio. This is emphasized explicitly by use of the two-parameter arctan function, rather than $\arctan(-U_S/Q_S)$.

3.3. Column density of the ISM from *Planck*

A standard optical measure of the column density of dust to a star is the colour excess $E(B - V)$. An estimate of the column density observed by *Planck* in the submillimetre is needed to check for the presence of a significant background beyond the star (Fig. 1). This independent estimate was based on the *Planck* map of the dust optical depth τ_S (and its error) at 353 GHz, at a resolution of $5'$, plus a calibration of τ_S into an equivalent reddening $E(B - V)_S$, using quasars: $E(B - V)_S \approx 1.49 \times 10^4 \tau_S$ (Planck Collaboration XI 2014).⁷

Based on the dispersion of the calibration, and the cross-checks with ancillary data, our adopted estimate for $E(B - V)_S$ should be accurate to about 30 % for an individual line of sight. Note that this uncertainty is not propagated directly into the final polarization ratios because $E(B - V)_S$ is not used in those calculations, but only for selection purposes (Sect. 5.3), whose robustness is explored below (Sect. 7).

4. Observations of polarization and extinction of starlight

Measurements of stellar polarization, here in the V band, are usually reported in terms of the degree of polarization, p_V , and the position angle, ψ_V , from which we can recover a representation of the observables in the HEALPix convention:

$$\begin{aligned} q_V &= p_V \cos 2\psi_V; \\ u_V &= -p_V \sin 2\psi_V. \end{aligned} \quad (4)$$

⁷ As discussed in Sect. 5, we are interested in the range $0.15 < E(B - V)_S < 1$ (or equivalently $0.87 < N_H < 5.8$ in units of 10^{21} cm^{-2} adopting the diffuse ISM conversion between $E(B - V)$ and N_H from Bohlin et al. 1978). Using the average opacity $\sigma_e(353) = \tau_{353}/N_H$ found over this range (Planck Collaboration XI 2014), together with this diffuse ISM conversion, results in a consistent calibration between $E(B - V)_S$ and τ_S . Furthermore, Planck Collaboration XI (2014) show that over the above range $E(B - V)_S$ compares favourably to estimates of colour excess based on stellar colours in the 2MASS data base (Skrutskie et al. 2006).

By definition, the optical depth is

$$\tau_V = A_V / 1.086. \quad (5)$$

The extinction A_V is found from the colour excess $E(B - V)$ through multiplication by the ratio of total to selective extinction, $R_V = A_V / E(B - V)$, either estimated from the shape of the multifrequency extinction curve or adopted as 3.1 as for the diffuse ISM (e.g., Fitzpatrick 2004) when such a measure is missing. Note that τ_V is not needed for $R_{P/P}$.

4.1. Polarization catalogue

We used the Heiles (2000) optical polarization catalogue, a compilation of several others (e.g., Mathewson & Ford 1971; Mathewson et al. 1978). This catalogue provides p_V and its uncertainty σ_{p_V} , together with $\psi_V \in [0^\circ, 180^\circ]$ in the IAU Galactic convention for 9286 stars. For data with $S/N > 3$, as will be imposed below, it is reasonable to use the Serkowski et al. (1975) approximation to the uncertainty σ_{ψ_V} in ψ_V :

$$\sigma_{\psi_V} = 28.65 \sigma_{p_V} / p_V \quad (6)$$

(e.g., Naghizadeh-Khouei & Clarke 1993). The catalogue also provides an estimate of the distance and colour excess to the star. However, the colour excess has too low a precision (0.1 mag) to be used here.

4.2. Extinction and colour excess catalogues

Accurate extinction data are needed both for the selection of stars (see Sect. 3.3) and for the calculation of $R_{S/V}$ (but not for $R_{P/P}$). We selected stars from various catalogues sequentially according to the accuracy of the technique used to derive $E(B - V)$ and A_V in the catalogue.

Using stellar atmosphere models, Fitzpatrick & Massa (2007) provide well-determined $E(B - V)$ and A_V measurements for 328 stars, 14 of which could be identified in the Heiles (2000) polarization catalogue *via* their catalogue identifiers (HD – Henry Draper, BD – Bonner Durchmusterung, CD – Cordoba Durchmusterung, or CPD – Cape Photographic Durchmusterung identifiers). This was the basis for what we refer to below as the “FM07 sample.” Similarly, from the Valencic et al. (2004) and Wegner (2002, 2003) extinction catalogues (derived with the more standard technique based on “unreddened” reference stars), we generated the VA04 and WE23 samples; note that we have removed stars in common with previously-defined samples, with the same order in priority of the samples. These three samples all contain measurements of both A_V and $E(B - V)$, providing an estimate of R_V , a useful diagnostic of the diffuse ISM where R_V is close to 3.1.

The Savage et al. (1985) catalogue provides measures of $E(B - V)$ to 1415 stars, 1085 of which were identified in the Heiles (2000) catalogue. Lacking a measure of R_V , we assumed the standard value for the diffuse ISM, $R_V = 3.1$; its uncertainty $\delta R_V = 0.4^8$ adds another uncertainty to our estimate of τ_V . Again removing stars in common with previous samples, we built the SA85 sample.

Using the high-quality photometry in the all-sky catalogue of Kharchenko & Roeser (2009), we were able to derive $E(B - V)$ and its uncertainty for more than 3000 stars present in the Heiles (2000) catalogue. As for the SA85 catalogue, we assumed $R_V =$

3.1 ± 0.4 for all stars. A few hundred stars overlapping the FM07, VA04, WE23, or SA85 samples allowed us to check the quality of our derivation of $E(B - V)$ (see Appendix B for details). Stars absent from other samples then form the KR09 sample.

5. Selection of stars

For each sample, we determined the subsample of stars to be used to calculate the polarization ratios $R_{S/V}$ and $R_{P/P}$ by applying four (sets of) selection criteria. We evaluate the dependence of our results on these criteria in Sect. 7.

5.1. S/N

The first criterion was to require a S/N higher than 3 for P_S and p_V , which propagates into an uncertainty in the position angle of less than 10° (Eq. 6). We also imposed a S/N higher than three for A_V (and consequently, τ_V), a quantity that might otherwise be poorly estimated.⁹ In emission, this condition is always met automatically for I_S when it is required for P_S .

Lines of sight where the column density is very low are too noisy in total extinction and in polarized emission to be used with confidence. We therefore further imposed $E(B - V) > 0.15$ and $E(B - V)_S > 0.15$. The latter criterion ensures that any uncertainties in the small corrections of I_{353} to I_S (Sect. 3.1) are unimportant.

5.2. Diffuse ISM

Our intent is to characterize dust polarization properties in the diffuse, largely atomic, ISM. To remove those lines of sight crossing denser molecular environments we used the *Planck* “type 3” CO map (Planck Collaboration XIII 2014) smoothed to $30'$ to impose the criterion

$$W_{\text{CO}} \leq 2 \text{ K km s}^{-1}. \quad (7)$$

The column density measure $E(B - V)_S$ can also be used to select statistically the diffuse atomic ISM: the higher $E(B - V)_S$, the higher the probability of sampling dense environments. We found the selection

$$E(B - V)_S \leq 1 \quad (8)$$

to be a good compromise between the size of the selected sample and the exclusion of dense environments (which are also generally characterized by a lower dust temperature, $T_{\text{dust}} \leq 17 \text{ K}$).

5.3. Compatibility between the column densities in the submillimetre and the optical

The selection on W_{CO} and $E(B - V)_S$ helps to remove some lines of sight with potential emission background beyond the star. This can be supplemented by comparing the *Planck* $E(B - V)_S$ with $E(B - V)$ for the star (see Fig. 1). Significant disagreement between the two column density estimates, whether an effect of different beams or an effect of the medium beyond the star, would mean that the polarization data cannot be compared usefully. The effect of slightly mismatched columns is mitigated somewhat by the normalization in $R_{S/V}$, which is a ratio of ratios; it is of heightened concern for $R_{P/P}$.

⁸ δR_V was set equal to the standard deviation of R_V in our final selected samples FM07, VA04, and WE23.

⁹ For the catalogues where R_V was not measured (SA85 and KR09), the assumed uncertainty $\delta R_V = 0.4$ introduced in Sect. 4.2 is ignored in the selection process, but not in the data analysis and fitting.

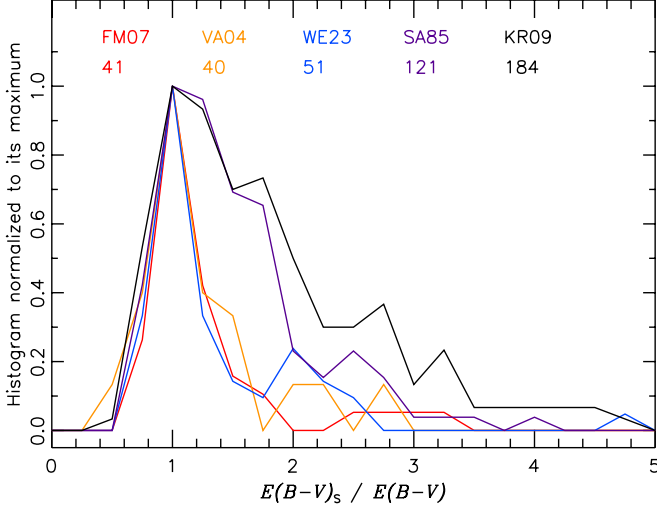


Fig. 2. Normalized histograms of the column density ratio R_{τ_S} for those lines of sight passing the first two selection criteria for S/N and diffuse ISM, for the independent FM07 (red), VA04 (orange), WE23 (blue), SA85 (mauve), and KR09 (black) samples. The number of stars in each sample is indicated.

We define the column density ratio between the submillimetre and the optical:

$$R_{\tau_S} = E(B - V)_S / E(B - V). \quad (9)$$

Figure 2 presents such a comparison in the form of a normalized histogram of R_{τ_S} for each sample. For the FM07, VA04, and WE23 samples the histograms correspond to what we would expect for lines of sight with little emission background beyond the star, namely a peak near $R_{\tau_S} \simeq 1$, and we take this as a first indication of the good quality of the $E(B - V)_S$ and $E(B - V)$ estimates. In Sect. 3.3 we estimated that for a given line of sight $E(B - V)_S$ might have a 30 % uncertainty and from the S/N criterion on τ_V (Sect. 5.1) the uncertainty in $E(B - V)$ is less than 33 %. These uncertainties would readily account for the width of the distribution about this peak.

Nevertheless, the SA85 and KR09 samples are not so well peaked, containing many lines of sight with $R_{\tau_S} \geq 2$. This might indicate a significant background beyond the star, which must in principle arise for some lines of sight. The stars in these independent samples, absent from the other more accurate samples, probe regions of the sky not represented by the other samples. Alternatively, for some lines of sight the dust opacity might be higher than for the diffuse ISM adopted here to derive $E(B - V)_S$ (see e.g., Martin et al. 2012; Roy et al. 2013), leading to an over-estimation.

Whatever the reason for this disagreement between $E(B - V)_S$ and $E(B - V)$, we need to be wary about including lines of sight with high R_{τ_S} in our analysis. Therefore, as a third criterion we removed all lines of sights with R_{τ_S} higher than a certain threshold.

To determine this threshold, we made use of the histograms of the difference in position angles in emission and in extinction:

$$\psi_{S/V} \equiv \frac{1}{2} \arctan [(U_S q_V - Q_S u_V), -(Q_S q_V + U_S u_V)]. \quad (10)$$

In the ideal case where measurements of emission and extinction probe the same medium, the polarization directions measured in

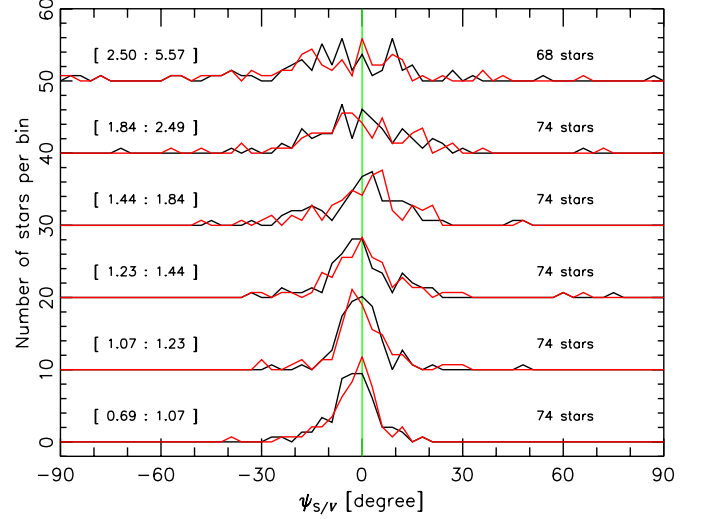


Fig. 3. Histograms of difference in position angles $\psi_{S/V}$ for successive intervals in column density ratio, R_{τ_S} , for data corrected (black) and not corrected (red) for the leakage of intensity into polarization. For the corrected version, each range in R_{τ_S} is indicated on the left, with the corresponding number of stars on the right. Only lines of sight of our five samples satisfying the first (S/N) and second (diffuse ISM) selection criteria have been used. For clarity, the histogram has been shifted upward by 10 units for each interval.

extinction and in emission should be orthogonal (e.g., Martin 2007). With Eq. 10, orthogonality corresponds to $\psi_{S/V} = 0^\circ$.¹⁰ Because the systematic presence of backgrounds beyond the stars would induce some deviations from orthogonality, we expect a decline of the quality of position angle agreement as R_{τ_S} increases.

This hypothesis is tested in Fig. 3, for lines of sight selected by only the first two criteria (S/N and diffuse ISM). The form of the histogram is observed to depend on the range considered for the column density ratio, R_{τ_S} . When the column densities agree ($R_{\tau_S} \simeq 1$), the histogram of $\psi_{S/V}$ is well peaked around zero, as expected. This agreement persists as long as R_{τ_S} is not too large, here below 1.6. Whether we correct for leakage (Sect. 3.1) or not has no effect on these conclusions. As a corollary, the agreement of column densities appears to be a good indicator of consistency between position angles, at least statistically.

Based on this discussion of Figs. 2 and 3, we defined our third selection criterion to be

$$R_{\tau_S} \leq 1.6. \quad (11)$$

It is conceivable that this selection tends, as a side effect, to select lines of sight with a low submillimetre opacity and so might bias our estimates. The use of an alternative column density ratio, based on the column density from H I 21 cm emission, is discussed in Sect. 7.

¹⁰ The expression for $\psi_{S/V}$ follows from the arctan addition rule as for Eq. 7 in Planck Collaboration Int. XIX (2014), with a minus sign before each argument allowing for the rotation by 90° of the polarization direction in emission as measured by ψ_S and an additional sign change in the first argument because $\psi_{S/V}$, like ψ_S and ψ_V , follows the IAU convention for angles, increasing from North through East (Eq. 3).

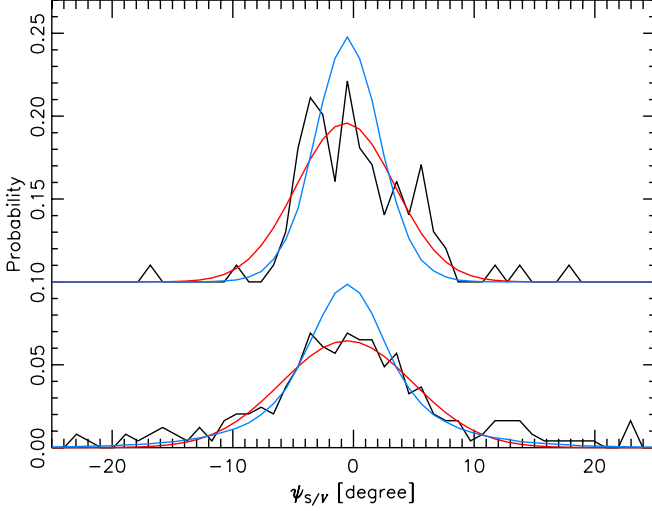


Fig. 4. Normalized histograms of the difference in position angles $\psi_{S/V}$ for lines of sight satisfying the three first selection criteria (S/N, diffuse ISM, and agreement in column density), for two selections on the S/N of P_S and p_V : S/N > 3 (Bottom); and S/N > 10 (Top). For clarity, the top set of curves has been shifted by 0.1. A Gaussian fit to each histogram is plotted in red. The blue curves show the expected distributions based on the noise estimates σ_{Q_S} , σ_{U_S} , σ_{q_V} , and σ_{u_V} ; compared to the measured distributions, these are slightly narrower and lack the larger outliers.

5.4. Consistency of polarization directions (orthogonality)

The fourth selection criterion is a check for the consistency *within the uncertainties* of the polarization directions in the visible and in the submillimetre, and is intended to remove outliers.

To acknowledge the non-ideal case in our sample of 249 stars selected by the above three criteria, we tested for consistency within a 2σ uncertainty plus allowance for a systematic error, $\Sigma_{\psi_{S/V}}$, due to potential effects of instrumental or astrophysical origin (e.g., the systematic presence of a small background beyond the star, beam effects):

$$|\psi_{S/V}| \leq 2\sigma_{\psi_{S/V}} + \Sigma_{\psi_{S/V}}, \quad (12)$$

$$\text{with } \sigma_{\psi_{S/V}} = \sqrt{\sigma_{\psi_S}^2 + \sigma_{\psi_V}^2}.$$

We merged the four histograms in Fig. 3 for $R_{\tau_S} \leq 1.6$, finding that the resulting histogram is well fitted by a Gaussian (red) with $\sigma = 5.5$ (Fig. 4). Repeating the same exercise, but with S/N ≥ 10 , the histogram is only approximately Gaussian, with $\sigma = 4.2$ for only 97 stars, providing an upper limit to $\Sigma_{\psi_{S/V}}$. Simulations based on the statistical uncertainties σ_{Q_S} , σ_{U_S} , σ_{q_V} , and σ_{u_V} are similar, with $\sigma = 3.9$ and 2.7 , respectively, but lack the outliers. To be conservative in our selection, we adopted $\Sigma_{\psi_{S/V}} = 2^\circ$, and note that this is used directly in Eq. 12, not in quadrature.

Figure 5 presents a comparison of the position angles for the sample of 249 stars selected above. As anticipated by the histograms of $\psi_{S/V}$ in Fig. 3, some lines of sight (plotted in red) are rejected by this fourth criterion.

The outliers in Figs 4 and 5 arise at least in part from systematic errors attributable to the small leakage of intensity into polarization that is imperfectly corrected in the March 2013 internal release of the *Planck* data (Sect. 3.1). Differing beams

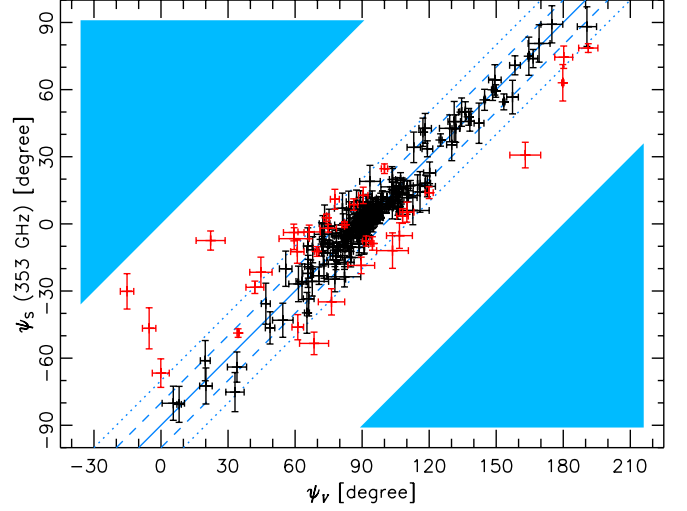


Fig. 5. Correlation plot of position angles in emission, ψ_S , and in extinction, ψ_V , for the merged sample, for lines of sight satisfying the first three selection criteria. Data for 34 lines of sight failing the fourth angle criterion are marked in red; those finally selected are in black. The central diagonal solid line indicates perfect agreement (orthogonal polarization pseudo-vectors), and other lines are for offsets of 10° (dashed) and 20° (dotted). Note that when the arithmetic difference in angles falls outside the allowed $\pm 90^\circ$ range for ψ_S (filled zones), the plotted ψ_V is adjusted by $\pm 180^\circ$ (Eq. 10).

and paths probed by submillimetre and optical measurements (Fig. 1) can also contribute.¹¹

Note that the final sample (plotted in black) covers a considerable range in position angle, i.e., the sample does not only probe environments where the orientation of the optical polarization is close to parallel to the Galactic plane ($\psi_V = 90^\circ$, $\psi_S = 0^\circ$). We will see in the following section that this dynamical range is essential for deriving the polarization ratios $R_{S/V}$ and $R_{P/p}$ using correlation analysis.

5.5. Galactic height

An alternative way to select lines of sight with little background is to select sufficiently distant stars. The Heiles (2000) catalogue contains estimates for the distance D to the star. This can be converted into an absolute Galactic height: $H = D |\sin b|$. Stars beyond the Galactic disk should have a reduced background and are therefore good candidates for using in our estimate of the polarization ratio. On the other hand, the most distant stars also probe the longest lines of sight where depolarization within the *Planck* beam will be the strongest (see Fig. 1), while not systematically affecting the degree of polarization in extinction. Although we did not adopt this as an additional criterion, we tested its impact in Sect. 7.1.

¹¹ Planck Collaboration Int. XIX (2014) have quantified the dispersion of the position angles measured in neighbouring *Planck* beams. The dispersion is anti-correlated with P_S/I_S (their Fig. 20) and dispersions comparable to the angle $\psi_{S/V}$ of the outliers in Fig. 4 occur statistically at low P_S/I_S , below a few percent. We find that $\psi_{S/V}$ also anti-correlates with P_S/I_S , suggesting that the same processes are responsible for the dispersion of the position angles in both extinction and emission at low fractional polarization.

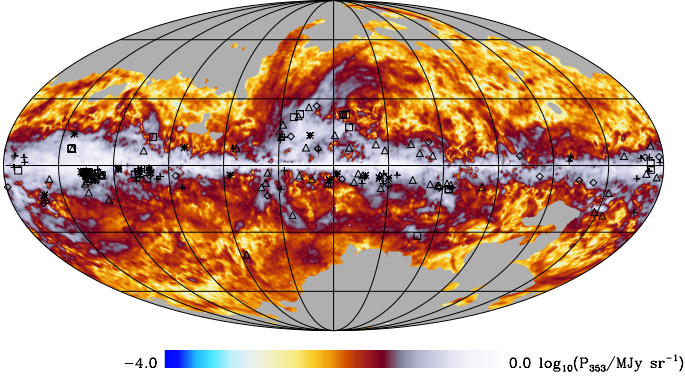


Fig. 6. Galactic lines of sight selected in our five independent samples: FM07 (squares), VA04 (asterisks), WE23 (diamonds), SA85 (crosses), and KR09 (triangles). The background image is of debiased polarized intensity, P_S , at a resolution of 1° (Planck Collaboration Int. XIX 2014) in a Mollweide projection centred on the Galactic centre. Near Galactic coordinates $(-134.7^\circ, -3.7^\circ)$ the selected stars are highly concentrated. Nevertheless, for $N_{\text{side}} = 2048$ there is only one pixel containing a pair of stars; there are two such pixels for $N_{\text{side}} = 1024$.

5.6. Selected sample of stars

Combining the four sets of criteria (regarding the S/N, the diffuse ISM, the agreement in column densities, and the consistency of position angles) for each sample we selected those lines of sight that would be suitable for a comparison of polarization efficiencies in the diffuse ISM. Table 1 presents the numbers of stars remaining in our sample after the selection criteria were applied in sequence. Starting from 9286 stars, we retain only 215. We assess the impact of this systematic reduction in Sect. 7 by relaxing our selection criteria.¹² Our full sample is spread between the different catalogues, thus avoiding any strong bias from any one in particular.

Table 1. Evolution of the number of stars remaining after successive selection criteria are applied.

| Selection criteria | FM | VA | WE | SA | KR | Total |
|-----------------------------|-----|-----|-----|-----|-----|-------|
| Heiles (2000) | | | | | | 9286 |
| $p_V/\sigma_{p_V} > 3$ | | | | | | 5579 |
| $P_S/\sigma_{P_S} > 3 @ 5'$ | | | | | | 3030 |
| $A_V/\sigma_{A_V} > 3$ | 128 | 245 | 338 | 575 | 980 | 2266 |
| Indep. samples | 128 | 147 | 207 | 324 | 653 | 1459 |
| Diffuse ISM | 41 | 40 | 51 | 121 | 185 | 438 |
| Column density | 34 | 30 | 36 | 69 | 80 | 249 |
| Position angles | 31 | 26 | 30 | 57 | 71 | 215 |

Figure 6 presents the Galactic coordinates of our selected stars in the five independent samples. Stars are more concen-

¹² For a consistent treatment, we use the same sample to examine $R_{P/p}$ as we use for $R_{S/V}$. However, we note that $R_{P/p}$ does not require the selection criterion of a high S/N for A_V ; furthermore, our unbiased correlation method (Sect. 6.1) can incorporate data with any S/N for P_S and p_V . Therefore, analysis of $R_{P/p}$ could be carried out with much larger sky coverage and better statistics. This will be exploited in a future paper dedicated to the question of variations of $R_{P/p}$ across the ISM. Lacking a measure of the column density probed in extinction through A_V , particular attention must be given to the possible effects of background contamination (Fig. 1).

trated in some local ISM regions of interest where the polarization fraction in the submillimetre is known to be high (Planck Collaboration Int. XIX 2014), in particular the Auriga-Fan region around $l = 135^\circ$ and $b = -5^\circ$ (accounting for about one third of our sample, see Table 3), the Aquila Rift around $l = 20^\circ$ and $b = 20^\circ$, and the Ara region at $l = 330^\circ$ and $b = -5^\circ$. The fact that all extinction catalogues provide data in these regions allows us to study local variations of $R_{S/V}$ with a limited bias (see Sect. 7.3).

6. Estimates of the polarization ratios

The polarization ratios, $R_{S/V}$ and $R_{P/p}$, defined in Eqs. 1 and 2, respectively, can in principle be obtained by correlating P_S with p_V and P_S/I_S with p_V/τ_V , respectively. However, the submillimetre polarized intensity, $P_S = \sqrt{Q_S^2 + U_S^2}$, involves non-linear operators (a quadratic sum and a square root), as does the polarization degree, p_V . In the presence of errors, these are biased estimates of the true values (Serkowski 1958; Wardle & Kronberg 1974; Simmons & Stewart 1985; see also Quinn 2012; Plaszczynski et al. 2014; Planck Collaboration Int. XIX 2014 and references therein). The polarization ratio, $R_{P/p}$, and the polarization efficiencies, P_S/I_S and p_V/τ_V – thus also the polarization ratio, $R_{S/V}$ – would be affected by the same problem. We revisit this in Sect. 6.3.

6.1. Correlation plots in Q and U for an unbiased estimate

In the ideal case where noise is negligible and the polarization pseudo-vectors in extinction and emission are orthogonal, from Eqs. 3 and 4 we have¹³ $Q_S/P_S = -q_V/p_V$ and $U_S/P_S = -u_V/p_V$, which yields

$$Q_S = -\frac{P_S}{p_V} q_V = -R_{P/p} q_V, \quad (13)$$

and the same for U . Introducing I_S and τ_V in the denominator on the left and right, respectively, and rearranging slightly, we obtain similarly

$$Q_S/I_S = -\frac{P_S/I_S}{p_V/\tau_V} q_V/\tau_V = -R_{S/V} q_V/\tau_V, \quad (14)$$

and the same for U . Therefore, the polarization ratios can be measured not only by correlating P_S with p_V and P_S/I_S with p_V/τ_V , but also by correlating their projections in Q and U .

We correlate in Q and U first separately, and then jointly. This approach has several advantages.

First, while P_S , p_V , P_S/I_S and p_V/τ_V are biased, their equivalents in Q and U are not biased.¹⁴

Second, the data in Q and U each present a better dynamic range than in P , because they can be both positive and negative and because they can vary from line of sight to line of sight if the position angle ψ changes, even while P and p (or equivalently P/I or p/τ) remain fairly constant. This allows for a better definition of the correlation¹⁵ and hence a better constraint on the slope, i.e., the polarization ratio.

¹³ Eq. 4 changes the signs of both q_V and u_V when the position angle ψ_V is changed by 90° .

¹⁴ Analysis using Q and U makes it possible to skip the S/N criteria for p_V and P_S , but not for A_V and I_S . This possibility is explored in Sect. 7.1.

¹⁵ Comparing Fig. 7 and 8, the Pearson correlation coefficients for the $R_{S/V}$ fit are -0.92 in Q and -0.88 in U as opposed to 0.74 in P , and for the $R_{P/p}$ fit are -0.93 in Q and -0.89 in U as opposed to 0.87 in P .

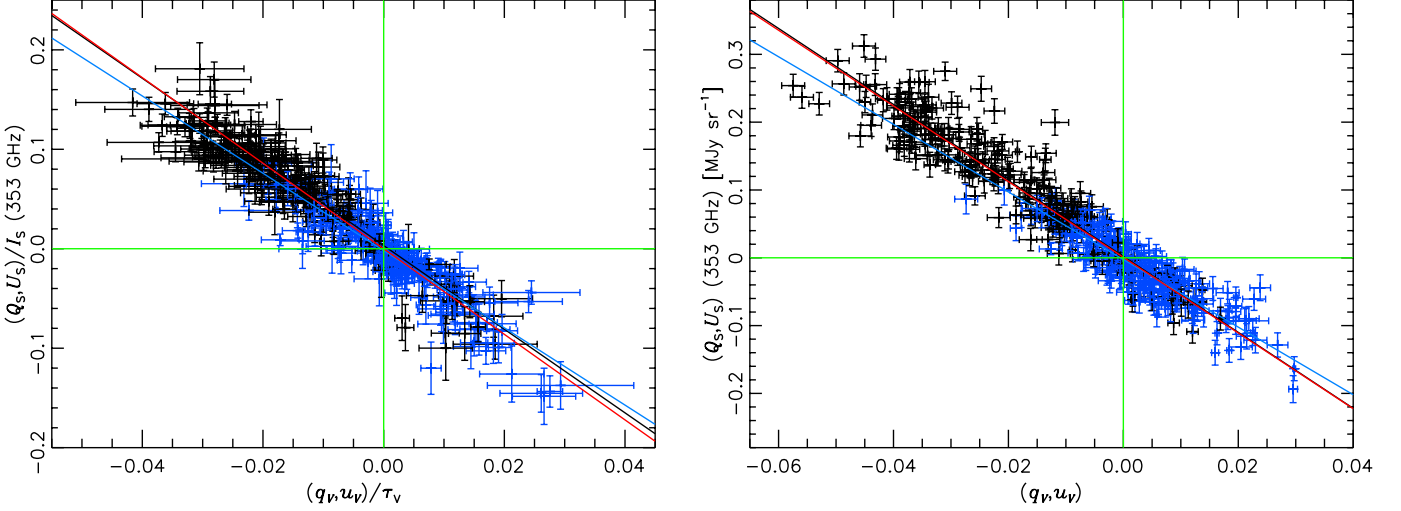


Fig. 7. *Left:* Correlation of polarization efficiencies in emission with those in extinction for the joint fit in Q (black) and U (blue). Using Eq. 16 the best linear fit (red line) has slope and y-intercept -4.30 ± 0.06 and 0.0000 ± 0.0006 , respectively. The Pearson correlation coefficient is -0.94 and $\chi_r^2 = 1.55$. *Right:* Correlation of polarized intensity in emission (MJy sr⁻¹) with the degree of interstellar polarization. Using Eq. 17, the best linear fit (red line) has slope and y-intercept (-5.58 ± 0.06) MJy sr⁻¹ and (0.0007 ± 0.0009) MJy sr⁻¹, respectively. The Pearson correlation coefficient is -0.96 and $\chi_r^2 = 2.39$. Lines for the independent fits to Q (black) and U (blue) are also shown.

Third, we can obtain two independent estimates of the polarization ratios from the slope of separate correlations for Q and for U . Under our hypothesis that for the samples of stars being selected the measured polarization in emission and extinction arises from the same aligned grains, these two estimates of the polarization ratio ought to be the same and the intercepts ought to be close to zero. In fact for the Q and U independent correlations analyzed using the scalar equivalent of Eq. 16 we find for the $R_{S/V}$ fit, respectively, slopes equal to -4.20 ± 0.10 and -3.89 ± 0.12 and y-intercepts equal to 0.0032 ± 0.0010 and -0.0018 ± 0.0008 , the latter both small compared to the dynamic range in Q and U (see Fig. 7). For the $R_{P/p}$ fit, this is (-5.60 ± 0.09) MJy sr⁻¹ and (-4.98 ± 0.14) MJy sr⁻¹ and y-intercepts equal to (0.0020 ± 0.0013) MJy sr⁻¹ and (-0.0025 ± 0.0013) MJy sr⁻¹. The uncertainties quoted were derived in the standard way from the quality of the fit. As reinforced by our bootstrapping analysis below (Sect. 6.2), the results of these independent fits are compatible with our hypothesis that the two correlations are measuring the same phenomenon, and furthermore reflect the quality of the selected data. See also Sect. 6.3 for a comparison with the fits in P .

Fourth, given this satisfactory consistency check, measuring the polarization ratios from the correlation of the joint data (Q, U) is both motivated and justified. We compute the linear ($y = ax + b$) best fit to the data by minimizing a χ^2 , which for the joint fit has the form¹⁶

$$\chi^2(a, b) = \sum_i V(a, b) M(a, b)^{-1} V(a, b)^T, \quad (15)$$

with

$$V(a, b) = (Q_S/I_S - a q_v/\tau_v - b, U_S/I_S - a u_v/\tau_v - b),$$

$$M(a, b) = \begin{pmatrix} C_{Q/I, Q/I} + a^2 \sigma_{q_v/\tau_v}^2 & C_{Q/I, U/I} \\ C_{Q/I, U/I} & C_{U/I, U/I} + a^2 \sigma_{u_v/\tau_v}^2 \end{pmatrix}, \quad (16)$$

¹⁶ The x and y coordinates can be inverted in the fitting routine without affecting the measure of the polarization ratio.

for the $R_{S/V}$ fit, and

$$V(a, b) = (Q_S - a q_v - b, U_S - a u_v - b),$$

$$M(a, b) = \begin{pmatrix} C_{QQ} + a^2 \sigma_{q_v}^2 & C_{QU} \\ C_{QU} & C_{UU} + a^2 \sigma_{u_v}^2 \end{pmatrix}, \quad (17)$$

for the $R_{P/p}$ fit. The calculation of the elements C of the noise covariance matrix, $[C]$, for the *Planck* data is presented in Appendix A.

Figure 7 presents the joint correlation of polarization in emission with that in extinction for the selected stars, both for $R_{S/V}$ (Left) and $R_{P/p}$ (Right). The slope of the correlation is -4.30 ± 0.06 and (-5.58 ± 0.06) MJy sr⁻¹, respectively. The correlation of the data is good (Pearson correlation coefficient -0.94 for $R_{S/V}$ and -0.96 for $R_{P/p}$). Values for the reduced χ^2 of the fit ($\chi_r^2 = 1.55$ for $R_{S/V}$ and 2.39 for $R_{P/p}$) are higher than expected given the large number of degrees of freedom (428), because the noise covariance matrix does not capture the systematic errors in the data, primarily from the leakage correction (see Sect. 3.1).

Note that the dynamic range of the data for the $R_{S/V}$ fit is influenced by the variation in the magnetic field structure (both in the plane of the sky and on the line of sight) and possibly in the grain alignment efficiency, while the range for the $R_{P/p}$ fit is also affected by the column density being probed (which has a dynamical range of a factor of about 6 in our sample, according to our selection on $E(B - V)_S$; see Sect. 5). The data for the correlation for $R_{P/p}$ do not depend on A_V and so, compared to the $R_{S/V}$ correlation, this correlation benefits from the lower noise in p_V than in A_V .¹⁷ Furthermore, the polarized intensity P_S is less contaminated by other backgrounds (e.g., CIB anisotropies) than is the total intensity I_S . Thus the Pearson correlation coefficient for the $R_{P/p}$ fit is slightly higher. However, despite this good correlation, χ_r^2 is actually higher for this fit, given the lower statistical

¹⁷ The polarization fraction p_V can be measured precisely even toward stars where the differential extinction $E(B - V)$ is not measurable (see the catalogue by Heiles 2000).

noise of the data being correlated; this is indicative of the presence of systematic errors. A few outliers are clearly identified in the $R_{P/P}$ fit, slightly increasing χ^2_r without affecting the fitted slope.

A small correction for leakage of intensity into polarization has been applied to the *Planck* polarization data used here (see Sect. 3.1). While this correction is imperfect, the alternative of ignoring this correction leaves systematic errors in the data. For the version of the data not corrected for leakage, we obtain figures similar to Fig. 7, for 195 selected stars, with Pearson correlation coefficients -0.94 and -0.95 and $\chi^2_r = 1.74$ and 2.78 , for $R_{S/V}$ and $R_{P/P}$, respectively. The mean slopes for the samples are $-R_{S/V} = -4.56 \pm 0.06$ and $-R_{P/P} = -5.88 \pm 0.06$ MJy sr $^{-1}$, significantly different compared to our previous estimates. This highlights that there is systemic uncertainty, albeit small, when using this generation of data for this analysis. The sensitivity of our result to the leakage correction is explored further in Sect. 7.

6.2. Parameters and uncertainties via bootstrapping

Because of the finite sample size and potential sensitivity to the exact membership in the samples, we used the technique of bootstrapping (Efron & Tibshirani 1993), in particular random sampling with replacement or case resampling, to carry out many instances of the fit, and then from these solutions we calculated the mean slope, the mean intercept, and their dispersions. The number of trials, 500, was large enough to ensure convergence of the results of resampling. The mean slope and intercept from bootstrapping for the $R_{S/V}$ fit are close to those from the original fits: for Q (before rounding), -4.21 ± 0.14 and 0.0031 ± 0.0026 from bootstrapping compared to -4.20 ± 0.10 and 0.0032 ± 0.0010 from the simple fit; for U , -3.90 ± 0.18 and -0.0018 ± 0.0011 , compared to -3.89 ± 0.12 and -0.0018 ± 0.0008 ; and for the joint fit, -4.30 ± 0.09 and 0.0000 ± 0.0010 , compared to -4.30 ± 0.06 and 0.0000 ± 0.0006 . Similar behaviours were obtained for $R_{P/P}$.

In the rest of the analysis in this paper we report the results from bootstrapping in terms of $R_{S/V}$ and $R_{P/P}$ (the negative of the values of the slopes) and to be conservative the dispersions were rounded to the upper first decimal (e.g., 0.12 gives 0.2) to give the statistical uncertainties quoted. In particular, from the joint fit $R_{S/V} = 4.3 \pm 0.1$, and $R_{P/P} = (5.6 \pm 0.2)$ MJy sr $^{-1}$.

6.3. Correlation plots in P

In Sect. 6.1 we derived $R_{S/V}$ and $R_{P/P}$ using joint correlation plots in Q and U rather than in the biased quantity P (see also footnote 12). However, our selection of P_S and p_V with $S/N > 3$ implies that the bias should not be too significant and it is possible to debias P at least statistically (the Modified Asymptotic debiasing method of Plaszczyński et al. 2014 was used; see also references in Sect. 6.1). This is confirmed by the correlation plot in Fig. 8 for debiased polarization efficiencies (which are almost identical to those for the original data). The submillimetre and optical data show a fairly good correlation, though, compared with Fig. 7, have a smaller dynamic range and a smaller Pearson correlation coefficient. We fit the slopes, forcing the fit to go through the origin unlike for the fits in Fig. 7. Whether with debiased data or not, the polarization ratios (from bootstrapping) are essentially identical: $R_{S/V} = 4.3 \pm 0.1$ and $R_{P/P} = (5.6 \pm 0.1)$ MJy sr $^{-1}$, and also the same as found in the preferred analysis in Fig. 7.

These good correlations confirm our initial idea that the polarization ratios can be obtained without limiting the analysis to

the case of optimal alignment (magnetic field in the plane of the sky, perfect alignment), and that the dependence of polarization efficiencies on the magnetic field orientation and on the dust alignment efficiency are similar in emission and in extinction. As a complement, we will show in Sect. 8.4 that a statistical analysis of the maximum polarization fractions seen in the optical and at 353 GHz gives a compatible result.

7. Robustness

In this section we investigate the robustness of the polarization ratios $R_{S/V}$ and $R_{P/P}$ with respect to the selection criteria defining the sample used in the analysis, the data used, the methodology, and the spatial location. We derive each time their mean values and uncertainties.

As a drawback, owing to its simplicity, $R_{P/P}$ involves systematic dependences on parameters such as the ambient radiation field, the submillimetre opacity of aligned grains, and the presence of a background beyond the star. Because P_S and p_V are proportional to the column density (of polarizing dust) probed with their respective submillimetre and optical observations, the correlation presented in Fig. 7 is potentially biased (an overestimate) if there is systematically a background beyond the stars selected (Fig. 1). Thanks to the normalization of P_S by I_S and p_V by τ_V , such dependences are weakened¹⁸ in the analysis of $R_{S/V}$.

7.1. Selection criteria

We explore the effects of varying the limits of the four selection criteria presented in Sect. 5. We do this one criterion at a time, with the others unchanged. We also examine other alternatives for defining the sample.

S/N The accuracy of the polarization degree in extinction data is not a limiting factor because the mean S/N is about 10 for the selected stars. Asking for a S/N threshold higher than 3 (Sect. 5.1) for P_S and for A_V could bias our estimates of $R_{S/V}$, which is proportional to these quantities. It would also exclude many diffuse regions where such a high S/N cannot be achieved at 5' resolution. Nevertheless, we find no significant variation of the polarization ratios when imposing $S/N > 1$ (265 stars, $R_{S/V} = 4.3 \pm 0.1$, $R_{P/P} = (5.6 \pm 0.2)$ MJy sr $^{-1}$) or $S/N > 10$ (85 stars, $R_{S/V} = 4.4 \pm 0.2$, $R_{P/P} = (5.6 \pm 0.2)$ MJy sr $^{-1}$).

Diffuse ISM The W_{CO} and $E(B - V)_S$ criteria (Eqs. 7 and 8 in Sect. 5.2) are responsible for the removal of lines of sight toward denser environments or toward the Galactic plane. Ignoring these criteria so that these stars are included gives $R_{S/V} = 4.1 \pm 0.2$ and $R_{P/P} = (5.8 \pm 0.2)$ MJy sr $^{-1}$, for 271 stars, an indication that the lines of sight added to the sample are contaminated by a weakly polarized submillimetre background. On the other hand, we can be more strict in our selection by imposing lower $E(B - V)_S$. For $E(B - V)_S \leq 0.5$, this yields a change in the opposite direction: $R_{S/V} = 4.5 \pm 0.2$ and $R_{P/P} = (5.5 \pm 0.2)$ MJy sr $^{-1}$ (103 stars).

Column density ratio The polarization ratio $R_{S/V}$ is, by construction, proportional to $E(B - V)$ and could therefore anticor-

¹⁸ For multiple grain populations the opacity and T_{dust} affecting I_S could be different than for P_S and so these effects might not cancel completely in the polarization efficiency P_S/I_S used in $R_{S/V}$.

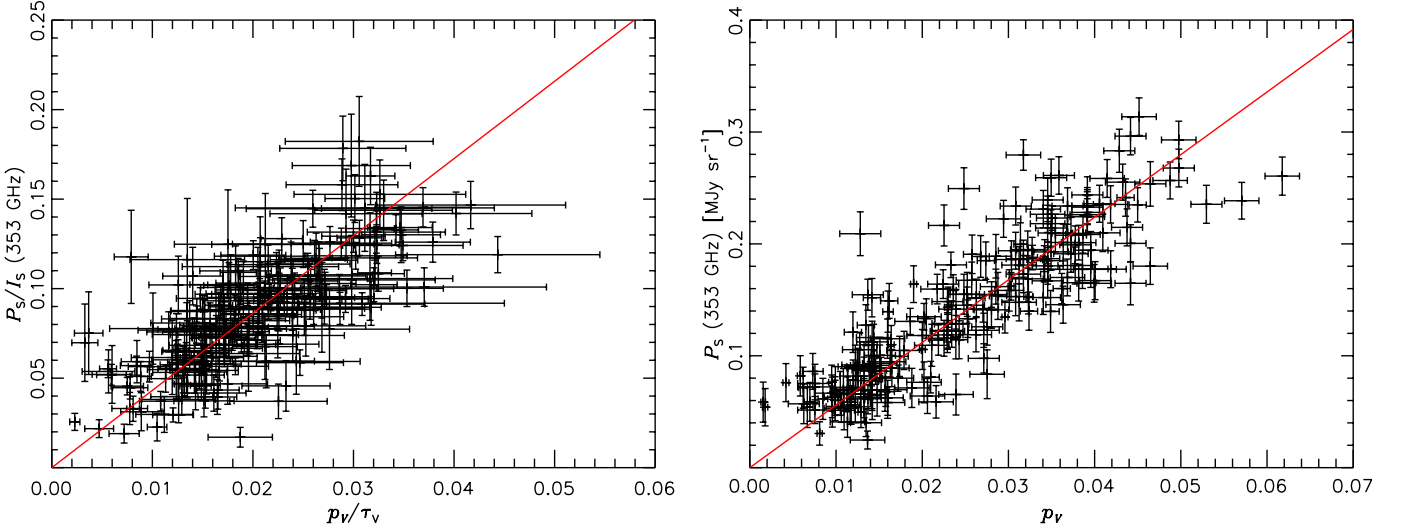


Fig. 8. *Left:* Correlation of debiased polarization efficiency in emission with that in extinction (Pearson coefficient 0.74). *Right:* Correlation of the debiased polarized emission (in MJy sr⁻¹) with starlight polarization degree (Pearson coefficient 0.87). The range corresponds to one quadrant in Fig. 7. The fits are forced to go through the origin and have slopes $R_{S/V} = 4.35 \pm 0.05$ ($\chi_r^2 = 1.73$) and $R_{P/p} = (5.62 \pm 0.04)$ MJy sr⁻¹ ($\chi_r^2 = 3.31$), respectively.

relate with R_{τ_s} . However, we do not find such dependance when varying the upper limit from 1.2 ($R_{S/V} = 4.3 \pm 0.2$, 121 stars) to 1.8 ($R_{S/V} = 4.3 \pm 0.1$, 240 stars). Going beyond the limits where angles agree, with upper limits of 2.0 and 3.0, yields the same value 4.2 ± 0.1 for the polarization ratio, for 262 and 311 stars, respectively.

Orthogonality If we become more restrictive in our selection based on the difference between position angles (Eq. 12 in Sect. 5.4), by requiring a 1σ agreement without the allowance for the systematic difference of 2° , our sample shrinks to 120 stars. The quality of the fit is preserved, as expected: $R_{S/V} = 4.4 \pm 0.2$ and $R_{P/p} = (5.7 \pm 0.2)$ MJy sr⁻¹.

Alternatively, if we base our selection on the 5.5° dispersion of the histogram of differences in position angle discussed in Sect. 5.4 (see also Fig. 4), say $|\psi_{S/V}| < 13^\circ$, 209 stars are selected and we find $R_{S/V} = 4.3 \pm 0.1$, $R_{P/p} = (5.6 \pm 0.2)$ MJy sr⁻¹.

Galactic height As discussed in Sect. 5.5, the Galactic height of the star can play a role, similar to that of the column density ratio R_{τ_s} , in selecting lines of sight with a low probability of background emission. Still requiring $R_{\tau_s} < 1.6$ and then selecting on $H > 100$ pc, $H > 150$ pc, and $H > 200$ pc, we find the same polarization ratios, $R_{S/V} = 4.2 \pm 0.2$ for 140, 88 and 52 stars, respectively. Selecting on $H > 100$ pc without selecting on the column density ratio, we obtain $R_{S/V} = 4.1 \pm 0.2$ (184 stars). Results for $R_{P/p}$ are also similar, with an average $R_{P/p} = (5.3 \pm 0.2)$ MJy sr⁻¹.

Selecting diffuse dust We can restrict our sample to lines of sight where the ratio of the total to selective extinction, R_V , is close to 3.1, its characteristic value for the diffuse ISM (e.g., Fitzpatrick 2004). Specifically, we exclude those lines of sight where R_V was not measured (SA85, KR09), and impose $2.6 < R_V < 3.6$. Our sample is then reduced to 72 stars and gives $R_{S/V} = 4.3 \pm 0.2$ and $R_{P/p} = (5.5 \pm 0.2)$ MJy sr⁻¹.

A similar selection can be made on the basis of the wavelength corresponding to the peak of the polarization curve in extinction, λ_{\max} , as taken from Serkowski et al. (1975). Imposing $0.5 \mu\text{m} < \lambda_{\max} < 0.6 \mu\text{m}$, we find $R_{S/V} = 4.4 \pm 0.2$ and $R_{P/p} = (5.5 \pm 0.3)$ MJy sr⁻¹, for 33 stars.

Radiance The radiance \mathcal{R} , i.e., the total power emitted by dust, is also a good measure of the column density observed in the submillimetre (Planck Collaboration XI 2014). However, unlike τ_s , this is most appropriate for very low column densities, $A_V < 0.5$, just outside the range defined by the first selection criterion (Sect. 5.1). Nevertheless, using \mathcal{R} instead of τ_s at 353 GHz to derive $E(B - V)_S$ and a column density ratio $R_{\mathcal{R}}$ as in Eq. 9 does not alter our selected sample size significantly and the derived $R_{S/V}$ is also the same. However, $R_{P/p}$ increases somewhat to (5.9 ± 0.2) MJy sr⁻¹, a possible signature of background contamination. This trend is indeed expected, because the radiance tends to underestimate the true column density (Planck Collaboration XI 2014).

21 cm emission In the diffuse ISM, $E(B - V)$ for the entire column can also be estimated from H I 21-cm emission. Following Planck Collaboration XI (2014), we use H I LAB data integrated in velocity (Kalberla et al. 2005), and assume the standard conversion factor from Bohlin et al. (1978) to define the equivalent submillimetre reddening $E(B - V)_{\text{HI}}$, and the corresponding column density ratio $R_{\text{HI}} = E(B - V)_{\text{HI}}/E(B - V)$. We obtain a histogram of R_{HI} similar to Fig. 2, though broader due to the lower resolution of the LAB survey ($36'$) and to the fact that $E(B - V)_{\text{HI}}$ might systematically underestimate the true dust column density by missing dust associated with any H₂ gas. Nevertheless, varying the upper limit for R_{HI} , we find the same values for $R_{S/V}$ as we do with R_{τ_s} . How $R_{P/p}$ and I_S/A_V depend on R_{HI} indicates the growing presence of a weakly polarized background with increasing R_{HI} : $R_{P/p}$ increases by 8 % and I_S/A_V by 30 % when R_{HI} varies from 1.2 to 3.0.

7.2. Data used

Here we test the sensitivity of our results to the choice of extinction catalogues and to the smoothing and original processing of the *Planck* data. The main sources of data uncertainty are, for the extinction data, the measure of A_V and, for the polarized emission data, the instrumental systematics related to the correction for the leakage of intensity to polarization (Sect. 3.1).

Extinction catalogues One important source of uncertainty in $R_{S/V}$ (not $R_{P/p}$) is the measure of the dust extinction in the optical, A_V . In Table 2 we summarize our results for each catalogue taken separately, independently of the others (i.e., we do not remove common stars). Although the catalogues neither share all of the same stars nor have the same extinction data for stars in common, the estimates obtained for $R_{S/V}$ and I_S/A_V are compatible. $R_{P/p}$ is independent of A_V , therefore of any extinction samples. Its variations among catalogues helps to constrain its statistical uncertainty, here less than 0.2 MJy sr^{-1} .

Table 2. $R_{S/V}$, $R_{P/p}$, and I_S/A_V with their uncertainties obtained with our bootstrap method for each sample taken independently of the others (common stars are *not removed*, unlike in our full sample; see Sect. 4.2).

| Sample | No. of stars | $R_{S/V}$ | $R_{P/p}$ (MJy sr ⁻¹) | I_S/A_V (MJy sr ⁻¹) |
|--------|--------------|---------------|--------------------------------------|--------------------------------------|
| FM07 | 31 | 4.1 ± 0.2 | 5.3 ± 0.3 | 1.32 ± 0.08 |
| VA04 | 52 | 4.5 ± 0.2 | 5.6 ± 0.3 | 1.25 ± 0.05 |
| WE23 | 53 | 4.1 ± 0.2 | 5.2 ± 0.2 | 1.25 ± 0.06 |
| SA85 | 102 | 4.5 ± 0.2 | 5.7 ± 0.2 | 1.33 ± 0.04 |
| KR09 | 135 | 4.3 ± 0.1 | 5.5 ± 0.2 | 1.33 ± 0.03 |

Smoothing In order to increase the S/N of the *Planck* polarization data and increase the quality of the correlations in Q and U , we chose to smooth our maps with a $5'$ FWHM Gaussian, making the effective map resolution $7'$. Because Q and U are algebraic quantities derived from a polarization pseudo-vector, the smoothing of polarization maps statistically tends to diminish the polarization intensity P_S , which would propagate into the polarization ratios $R_{S/V}$ and $R_{P/p}$. Using the raw (not smoothed) data, or data smoothed with a beam of $3'$ and $8'$ (keeping the same sample as was selected using data smoothed with a $5'$ beam to allow for an unbiased comparison), we find $R_{S/V} = 4.1 \pm 0.2$, 4.3 ± 0.1 , and 4.4 ± 0.1 , respectively, revealing a slight increasing trend, which is however not significant. This trend is also observed with $R_{P/p}$ ($R_{P/p} = (5.3 \pm 0.3) \text{ MJy sr}^{-1}$, $(5.6 \pm 0.2) \text{ MJy sr}^{-1}$, and $(5.7 \pm 0.1) \text{ MJy sr}^{-1}$, respectively). Note that the mean values of $R_{S/V}$ and $R_{P/p}$ could still be underestimated owing to depolarization in the *Planck* beam, which does not have a counterpart in the visible measurement (see Fig. 1); however, this effect should be small and within the uncertainties.

Zodiacal emission Removing zodiacal emission, or not, in deriving I_S (Sect. 3.1) does not affect our result, with $R_{S/V} = 4.3 \pm 0.1$ and $R_{P/p} = (5.6 \pm 0.2) \text{ MJy sr}^{-1}$ in both cases.

Leakage correction Running the analysis with the version of the original data, *not* corrected for the leakage of intensity into

polarization, 195 stars are selected and we find $R_{S/V} = 4.6 \pm 0.2$ and $R_{P/p} = (5.9 \pm 0.2) \text{ MJy sr}^{-1}$, systematic changes of $+0.3$ and $+0.3 \text{ MJy sr}^{-1}$ compared to our adopted value. The correction of *Planck* polarization data for this leakage is therefore, in its current version, a main source of systematic uncertainty in $R_{S/V}$ and $R_{P/p}$, though perhaps not as much as 0.3 or of the same sign.

Contamination by CMB polarization at 353 GHz Following the approach in Planck Collaboration Int. XXII (2014) approach, we can remove the CMB patterns in intensity and polarization from the 353 GHz maps by subtracting the 100 GHz (I, Q, U) maps in CMB thermodynamic temperature units. This method unfortunately adds noise to the 353 GHz maps, and is therefore used only as a check. It also has the drawback of subtracting a fraction of dust emission that is present in the 100 GHz channel. However, dust is then subtracted both in intensity and in polarization, though perhaps not proportionally to the polarization fraction at 353 GHz (however, this is a second order effect). With this 100 GHz-subtracted version of Q and U , we obtain $R_{S/V} = 4.3 \pm 0.1$ and $R_{P/p} = (5.5 \pm 0.2) \text{ MJy sr}^{-1}$, for 208 stars.

7.3. Spatial dependence

Galactic latitude We find mild variations of the polarization ratios between the two hemispheres: $R_{S/V} = 4.1 \pm 0.2$ and $R_{P/p} = (5.2 \pm 0.3) \text{ MJy sr}^{-1}$ for the northern Galactic hemisphere, and $R_{S/V} = 4.4 \pm 0.2$ and $R_{P/p} = (5.7 \pm 0.2) \text{ MJy sr}^{-1}$ for the southern.

Polarization ratios could also depend on the latitude of stars as it is indicative of potential backgrounds. Selecting high latitude stars from both hemispheres ($|b| > 6^\circ$, 84 stars) to limit the presence of backgrounds, we find $R_{S/V} = 4.3 \pm 0.2$, $R_{P/p} = (5.4 \pm 0.3) \text{ MJy sr}^{-1}$, and $I_S/A_V = (1.28 \pm 0.07) \text{ MJy sr}^{-1}$. For low latitude stars ($|b| \leq 6^\circ$, 131 stars), $R_{S/V} = 4.3 \pm 0.1$, $R_{P/p} = (5.6 \pm 0.2) \text{ MJy sr}^{-1}$, and $I_S/A_V = (1.26 \pm 0.05) \text{ MJy sr}^{-1}$, with no indication of any contamination by backgrounds.

Variations from region to region The polarization ratios that we derived in previous sections are an average over the sky. Here we explore the possibility of variations of $R_{S/V}$ and $R_{P/p}$ between different regions of the sky. Table 3 presents the polarization ratios for three regions, among them the Fan which contains almost one third of our selected stars; these results are close to the overall average. If we select all stars except those from the Fan, we find $R_{S/V} = 4.4 \pm 0.2$ and $R_{P/p} = (5.7 \pm 0.2) \text{ MJy sr}^{-1}$. We conclude that our total sample is not biased by any particular region.

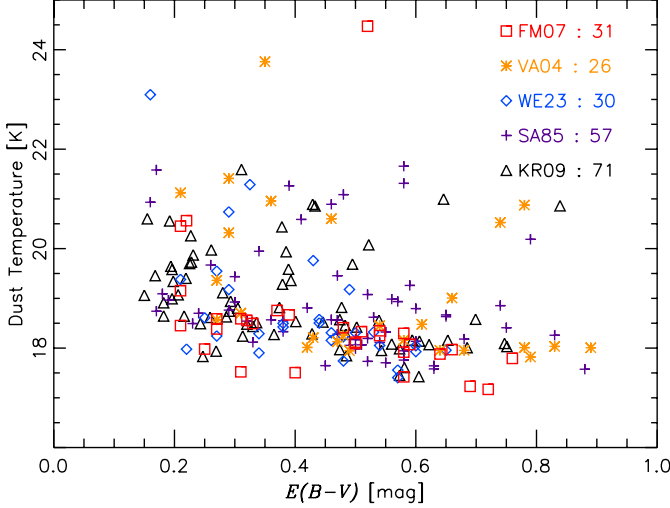
Table 3 also presents the polarization ratios for two other regions in the local ISM where stars in our sample are more concentrated (see Fig. 6): the Aquila Rift, and the Ara region (Planck Collaboration Int. XIX 2014). The polarization ratios appear to have regional variations (± 0.5 for $R_{S/V}$, $\pm 0.5 \text{ MJy sr}^{-1}$ for $R_{P/p}$) that are larger than the differences induced by the correction of the data for leakage of intensity into polarization, suggesting possible true cosmic variance of the polarization ratios. Nevertheless, these variations are small (around 10%) and their significance is difficult to assess.

7.4. Relationship to thermal dust temperature

Figure 9 shows the distribution in the dust temperature (T_{dust}) – column density (as measured by $E(B - V)$) plane. The dust tem-

Table 3. Values of $R_{S/V}$ and $R_{P/p}$ in specific regions.

| Region | Longitude [deg] | Latitude [deg] | No. stars | $R_{S/V}$ | $R_{P/p}$ [MJy sr ⁻¹] | I_S/A_V [MJy sr ⁻¹] | $\langle T_{\text{dust}} \rangle$ [K] |
|-------------|--------------------|-------------------|-----------|---------------|--------------------------------------|--------------------------------------|--|
| Fan | [125° : 140°] | [-8°5 : -1°5] | 71 | 4.3 ± 0.2 | 5.5 ± 0.2 | 1.19 ± 0.03 | 18.3 |
| Aquila Rift | [320° : 360°] | [+10° : +35°] | 18 | 4.8 ± 0.3 | 5.4 ± 0.3 | 1.26 ± 0.17 | 19.4 |
| Ara | [340° : 40°] | [-12° : -2°0] | 27 | 4.1 ± 0.3 | 6.0 ± 0.4 | 1.48 ± 0.07 | 20.7 |


Fig. 9. *Planck* line of sight dust temperature T_{dust} (Planck Collaboration XI 2014) and the column density to the star, $E(B - V)$, for the independent samples.

perature, from Planck Collaboration XI (2014), characterizes the spectral energy distribution of the combined emission I_S from all dust components in the column of dust along the line of sight. Note that the parameter T_{dust} has no direct connection to the sample selection. The ranges of $E(B - V)$ and T_{dust} are considerable for each sample. In this plane, there is a band showing a slight anti-correlation of T_{dust} and $E(B - V)$; there are also several lines of sight with $T_{\text{dust}} \approx 21$ K but with a range of $E(B - V)$. Here we explore the possible dependencies of $R_{S/V}$, $R_{P/p}$, and I_S/τ_V on T_{dust} .

Figure 10 shows how the ratios $R_{S/V}$, $R_{P/p}$, and I_S/A_V depend on the dust temperature, for data with and without the correction for leakage of intensity into polarization. The data are binned, each bin containing the same number of stars. Successive bins are placed such that each bin shares half of its stars with its left neighbour and half with its right, so that any trend is smoothly sampled. For the data corrected for leakage, $R_{S/V}$ does not depend much on the dust temperature for $T_{\text{dust}} < 19$ K, but possibly decreases for higher temperatures. The trend with T_{dust} , stronger for data not corrected for leakage, arises from stars at low Galactic latitude. Any trend is very small, only $\pm 10\%$ over this range in T_{dust} , and not definitive, owing to the uncertainties in the leakage correction.

The dependence of $R_{P/p}$ on T_{dust} is rather flat, and does not seem to follow the blackbody trend that is seen for I_S/A_V . Recall that T_{dust} is derived by fitting the SED of I_S and so the blackbody trend represented by the blue line is expected for I_S/A_V , but not necessarily for $R_{P/p}$. Whether the variations in $R_{P/p}$ agree with this trend bears on the question of whether the polarizing grains have a distinctive equilibrium temperature. As described

in Planck Collaboration XII (2014) and Planck Collaboration Int. XVII (2014), the submillimetre opacity drives the cooling of the grains and sets the equilibrium temperature; changes in the opacity of the polarizing grains could be poorly correlated with the changes in the total opacity and thus hide this trend.

7.5. Adopted mean values and uncertainties for $R_{S/V}$ and $R_{P/p}$ in the diffuse ISM

On the basis of the various results presented in the previous sections, we adopt the following values for the polarization ratios in the diffuse ISM:

$$R_{S/V} = (P_S/I_S)/(p_V/\tau_V) = 4.3 \pm 0.2 \text{ (stat.)} \pm 0.4 \text{ (syst.)}. \quad (18)$$

The statistical uncertainty is representative of the standard deviation of the histogram of $R_{S/V}$ found by bootstrap analysis in the many robustness tests. The systematic error gathers all potential contributions, but is dominated by our incomplete knowledge of the small correction of *Planck* data for leakage of intensity into polarization (Sect. 3.1).

The polarization ratio $R_{P/p}$ has been shown to have systematic variations similar to those for $R_{S/V}$. From the robustness analysis (Sect. 7), we adopt

$$R_{P/p} = P_S/p_V = [5.6 \pm 0.2 \text{ (stat.)} \pm 0.4 \text{ (syst.)}] \text{ MJy sr}^{-1}. \quad (19)$$

The statistical uncertainty from the bootstrap is again rather small. Uncertainties in $R_{P/p}$ are dominated by systematic errors, namely from uncertainties in the leakage correction and from the tendency to overestimate $R_{P/p}$ in the presence of backgrounds beyond the stars.

The corresponding total intensity per unit magnitude in the V band, I_S/A_V , is obtained by the direct calculation $I_S/A_V = R_{P/p}/R_{S/V}/1.086 = 1.2 \text{ MJy sr}^{-1}$, with an uncertainty ± 0.1 .

To help in constraining dust models, we provide the mean spectral energy distribution (SED) for the lines of sight in our sample in the form of a modified blackbody fit to the data (Planck Collaboration XI 2014): $T_{\text{dust}} = 18.5$ K; $\beta_{\text{FIR}} = 1.62$; and a dust opacity at 353 GHz, $\tau_S/A_V = 2.5 \times 10^{-5} \text{ mag}^{-1}$ after a 10 % colour correction (Planck Collaboration IX 2014).

8. Discussion

Our measurement of the polarization ratios $R_{S/V}$ and $R_{P/p}$ provide new constraints on the submillimetre properties of dust. In fact, in anticipation of results from *Planck*, $R_{S/V}$ for the diffuse ISM has already been predicted in two studies.

8.1. $R_{S/V}$ from dust models

Martin (2007) discussed how P_S/I_S at 350 GHz can be predicted by making use of what is already well known from dust models of optical (and infrared and ultraviolet) interstellar polarization and extinction. From that study, the polarization ratio of interest here, $R_{S/V}$, can be recovered by dividing the estimated values

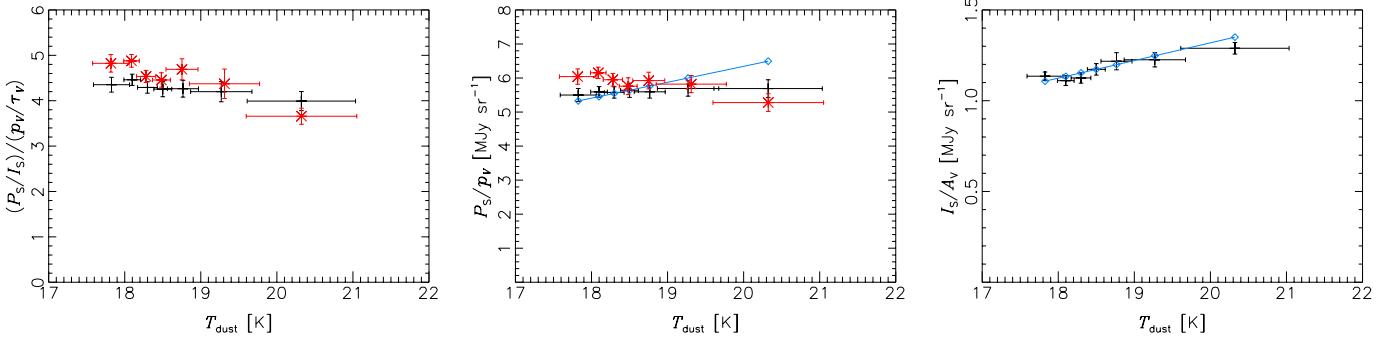


Fig. 10. *Left:* Variation of mean $R_{S/V}$ as a function of the mean T_{dust} (each plotted with the standard deviation) in each bin. Two versions of the *Planck* data have been used: with (black crosses) and without (red asterisks) correction for leakage of intensity into polarization, using 53 and 48 stars per bin, respectively (see text for the way bins were built). *Middle:* The same, but for $R_{p/p}$. *Right:* The same, but for I_S/A_V . The blue lines in the middle and right panels model the potential blackbody dependence of $R_{p/p}$ and I_S on T_{dust} .

of P_S/I_S in the last row of his Table 2, first by 100 (to convert from percentages) and then by 0.0267, the value of p_V/τ_V on which the table was based. For example, for aligned silicates in the form of spheroids of axial ratio 1.4, the entry is 9.3, so that $R_{S/V} = 3.5$. Similar values are obtained for other shapes and axial ratios, because changes in these factors affect both optical and submillimetre polarization. Sources of uncertainty in this prediction include whether imperfect alignment reduces the polarization equally in the optical and submillimetre (as was assumed), how the optical extinction is modelled, whether by aligned or by randomly oriented grains ($\pm 25\%$), and the amount by which the submillimetre fractional polarization is reduced by unpolarized emission from carbonaceous grains in the model; adopting a dilution closer to that in the Draine & Fraisse (2009) mixture discussed below could raise $R_{S/V}$ to about 4.5. Thus, given these uncertainties, the prediction of $R_{S/V}$ is in reasonable agreement with what has now been observed.

Draine & Fraisse (2009) also made predictions of P_S/I_S for mixtures of silicate and carbonaceous grains, where again the dust model parameters (size distributions, composition, alignment, etc.) were constrained by a detailed match to optical extinction and polarization curves, with the normalization $p_V/\tau_V = 0.0326$. According to their Fig. 8, at 350 GHz P_S/I_S is about 13–14 % for models in which only the silicate grains are aspherical and aligned (axial ratio 1.4–1.6), and about 9–10 % for models in which both silicate and carbonaceous grains are aspherical and aligned. Dividing as above yields $R_{S/V} = 4.1$ and 2.9, respectively.

These are challenging calculations that encounter similar issues to those discussed in Martin (2007), including the question of dilution if the basic properties of the building block materials, such as the submillimetre opacity, are not precisely known. In the Draine & Fraisse (2009) study P_S/N_H , unlike I_S/N_H , is rather independent of the models, as can be seen from their Figs. 8 and 7, respectively. We infer that the different predictions presented in Draine & Fraisse (2009) for P_S/I_S are not related to a variation of the dust polarization properties among models (with or without graphite aligned), but to the poor fit of the total SED obtained with models where graphite grains are spherical and not aligned. Briefly, P_S/I_S is predicted to be 30 % higher when graphite grains are spherical mainly because the total intensity I_S is 30 % lower than the data; there is a discrepancy with the dilution. All such models with a precise fit to the submillimetre

tre intensity data would predict P_S/I_S about 10 %, and therefore $R_{S/V}$ about 3.5.

While the results are suggestive, we feel that it is not yet possible to choose definitively between different models. Therefore, further constraints would be helpful.¹⁹

8.2. $R_{p/p}$ and I_S/A_V from dust models

The polarization ratio $R_{p/p}$ is a more direct and easier-to-model observational constraint. Unlike for $R_{S/V}$, one does not need to model the extinction and emission of non-aligned or spherical grain populations. Model predictions for $R_{p/p}$ will depend not only on the size distribution, optical properties, and shape of the aligned grain population, but also on the radiation field intensity, which affects P_S without affecting p_V . Because $R_{p/p}$ is not a dimensionless quantity like $R_{S/V}$, it provides a new constraint on grain models, i.e., models that are able to reproduce $R_{S/V}$ will not automatically satisfy $R_{p/p}$.

From the Draine & Fraisse (2009) prediction of P_S/N_H we measure $v_S P_S/N_H \approx 1.0 \times 10^{-11}$ W sr⁻¹ per H at 353 GHz. In the optical the same models produce $p_V/N_H \approx 1.4 \times 10^{-23}$ cm² per H (their Fig. 6, taking into account their Erratum). These can be combined to give $R_{p/p} \approx 2.2$ MJy sr⁻¹. This value is significantly lower than our empirical results, by a factor 2.5.

As this example illustrates, there is potentially great diagnostic power in focusing directly on the polarization properties alone; $R_{p/p}$ describes the aligned grain population and so is important, along with $R_{S/V}$, for constraining and understanding the full complexity of grain models.

Complementing the discussion in Sect. 8.1, from the Draine & Fraisse (2009) prediction of I_S/N_H we measure $v_S I_S/N_H \approx 0.7\text{--}1.1 \times 10^{-10}$ W sr⁻¹ per H at 353 GHz. In the optical the same

¹⁹ Hoang et al. (2013) recently predicted P_S/I_S for the only two stars that show a significant polarization of their 220-nm UV bump, HD 197770 and HD 147933-4. These stars, part of the FM07 catalogue, were eventually *not selected* in our final sample: HD 197770 satisfies all criteria except for the CO integrated emission ($W_{\text{CO}} \approx 6$ K km s⁻¹); the line of sight toward HD 147933-4 includes a dense molecular medium ($W_{\text{CO}} \approx 8$ K km s⁻¹, $R_V = 4.3$) with a significant background beyond the star ($R_{\tau_S} \approx 2$). The polarization fraction P_S/I_S for the entire line of sight toward HD 197770 and HD 147933-4 is measured to be 5.5 % and 7.9 %, respectively. These are a factor of about 2 below the values 11 % and 14 % that they predicted, albeit that their predictions are for that part of the line of sight that is in front of the star.

models produce $\tau_V/N_H \approx 4.5 \times 10^{-22} \text{ cm}^2 \text{ per H}$ (their Fig. 4). These can be combined to give $I_S/\tau_V \approx 0.5\text{--}0.8 \text{ MJy sr}^{-1}$, after a colour correction by 10 %, taking into account the width of the 353 GHz *Planck* band (Planck Collaboration IX 2014). These values are significantly lower than our empirical results, by a factor 1.5–2.4, depending on the model.²⁰ The magnitude of the discrepancy in polarized emission is up to 30 % higher than it is for intensity.

8.3. The frequency dependence of P_S and P_S/I_S

As pointed out by Martin (2007), to help separate and characterize the components, it is useful to measure the spectral dependence of P_S and I_S directly, for comparison with models. This has been accomplished by Planck Collaboration Int. XXII (2014) using *Planck* and *WMAP* data at frequencies extending lower than examined in this paper, from 353 GHz down to 70 GHz. Over the HFI range between 353 GHz and 100 GHz, $\beta_{\text{mm}}^P = 1.63 \pm 0.03$ for P_S . This too is a new constraint on polarizing grain models.

For submillimetre emission from the aligned grain component, there are reasonable models in which P_S/I_S can be quite independent of frequency (i.e., P_S and I_S have the same spectral index β). However, as in the composite models above, there can be another contribution to I_S from unaligned grains. Therefore, if this diluting component has a different spectral index, then the net polarization fraction P_S/I_S observed will be frequency dependent. This is illustrated by a plausible toy model in Martin (2007). The models of Draine & Fraise (2009) with aligned silicates and unaligned carbonaceous particles show the same phenomenon, with P_S/I_S increasing toward lower frequencies. This arises because the silicate component has $\beta = 1.7$, a flatter spectrum than for the carbonaceous material (graphite, with $\beta = 2$).

However, this is not a definitive signature of a mixed model with silicates and carbonaceous grains. In fact, carbonaceous materials might have flatter spectra (e.g., as adopted in the DustEM model, Compiègne et al. 2011) and silicates might have $\beta = 2$,²¹ in which case P_S/I_S would decrease toward lower frequencies. Nevertheless, one can appreciate the potential to constrain the dust models.

Planck Collaboration Int. XXII (2014) also found $\beta_{\text{mm}}^I = 1.52 \pm 0.02$ for I_S so that, in combination with the independently measured β_{mm}^P , the polarization fraction P_S/I_S decreases slightly toward lower frequencies; this decrease continues further to 70 GHz. This is a constraint on models of the grains, polarizing and non-polarizing together.

8.4. $R_{S/V}$ and its relationship to the maximum observed polarization efficiencies

For a given dust model, including the grain shape, the maximum polarization efficiency that can be observed corresponds to the ideal case of optimal dust alignment: the magnetic field lies in the plane of the sky, has the same orientation (position angle) along the line of sight, and the dust alignment efficiency with respect to the field is perfect. The maximum $p_V/\tau_V \approx 3\%$ observed in extinction (corresponding to $p_V \leq 9\% E(B-V)$, Serkowski et al. 1975), is supposed to be close to this ideal case. For our selected sample of lines of sight, Fig. 11 (left panel) shows this “classical” envelope and the corresponding envelope ($P_S/I_S = 3\% \times R_{S/V} = 12.9\%$) transferred to emission (right panel).

We have also investigated the upper envelope that might be derived independently from the emission data. At a resolution of 1° *Planck* HFI has revealed regions with P_S/I_S greater than 20 % (Planck Collaboration Int. XIX 2014), albeit for only a very small fraction (0.001) of lines of sight, toward local diffuse clouds. This value, which is already a high envelope, might have been even larger were it at the finer resolution of starlight measurements. Combined with the 3 % limit from stars, this would apparently imply $R_{S/V} > 6$, significantly higher than our mean value $R_{S/V} = 4.3$. However, for statistical reasons, these two estimates of $R_{S/V}$ cannot be compared straightforwardly: *Planck* statistics are based on (almost) full-sky data, while those of Serkowski et al. (1975) are based on less than 300 stars. The upper limit of 3 % for p_V/τ_V is therefore certainly underestimated.²²

A more consistent statistical comparison can be sought. Analyzing Fig. 9 of Serkowski et al. (1975) and limiting our analysis to stars satisfying $0.15 < E(B-V) < 1$ similar to our selection criterion (Sect. 5.2), the upper envelope $p_V \leq 9\% E(B-V)$ is approximately the 97 % percentile of $p_V/E(B-V)$ (in this interval of $E(B-V)$, 8 stars out of about 250 lie above this envelope). The corresponding 97 % percentile of P_S/I_S in our selected sample is $P_S/I_S = 15\%$ (7 stars out of 215 above that line). Obtaining the 97 % percentile of the full *Planck* map is not an easy task, because noise makes it resolution dependent (Planck Collaboration Int. XIX 2014) and any selection criterion on the S/N of P_S would bias the analysis. Nevertheless, we can obtain a reasonable estimate by smoothing the 353 GHz maps with a Gaussian of $5'$ and selecting those pixels with $0.15 < E(B-V)_S < 1$. The 97 % percentile of P_S/I_S (after debiasing) in this sample of pixels is found to be about 14%. Combining these estimates based on consistent percentiles implies $R_{S/V}$ in the range 4.4–4.8, not incompatible with our direct result, especially if there were regional variations, as explored in Sect. 7.3.

9. Conclusion

Comparison of submillimetre polarization, as seen by *Planck* at 353 GHz, with interstellar polarization, as measured in the optical, has allowed us to provide new constraints relevant to dust models for the diffuse ISM. After carefully selecting lines of sight in the diffuse ISM suitable for this comparison, a correlation analysis showed that the mean polarization ratio, defined

²⁰ By fitting *Planck* intensity maps with the Draine & Li (2007) dust model, Planck Collaboration Int. XXV (2014) derived A_V maps that were found to be overestimated compared to data by a factor 1.9; alternatively, normalizing the models to the observed A_V , the submillimetre emission is underpredicted by a factor 1.9, like in Draine & Fraise (2009).

²¹ The spectral properties of “astronomical silicate” used by Draine & Fraise (2009) had been modified away from $\beta = 2$ by Li & Draine (2001) in a plausible way so that, in combination with their choice of carbonaceous grains, graphite, they could match the observed low frequency spectral energy distribution of the high latitude diffuse ISM. More generally, outside the context of this specific model, this modification might not be required.

²² This upper limit is also exceeded in some localized molecular environments (e.g., Andersson & Potter 2007), but those are not considered here.

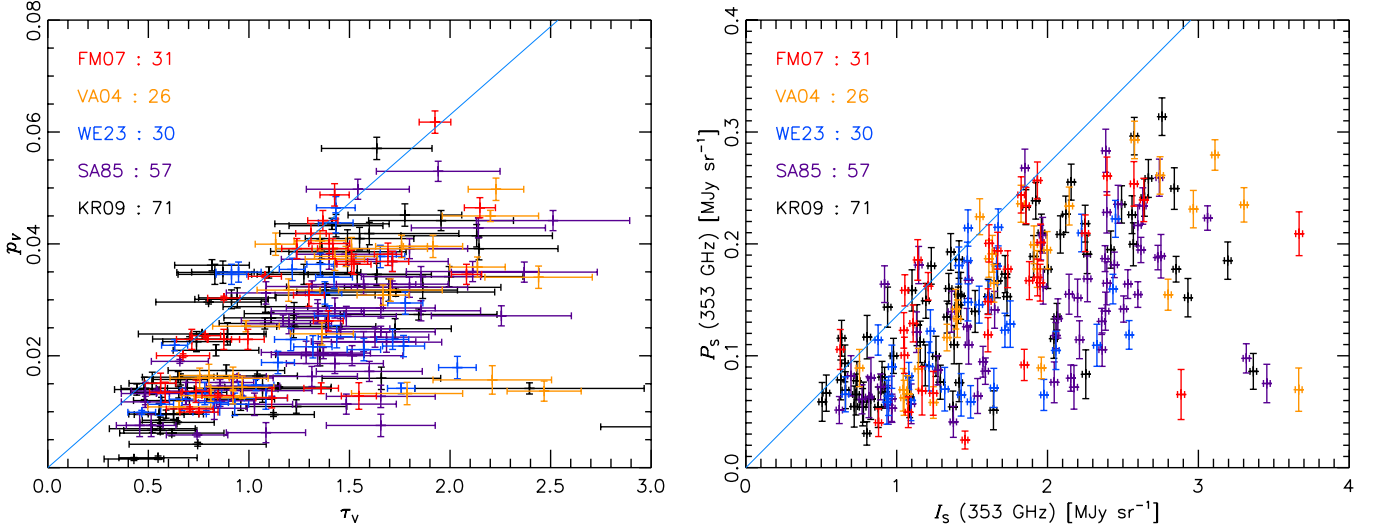


Fig. 11. Scatterplots of data for the selected lines of sight. Polarization degree p_V and intensity P_S were debiased with the Modified Asymptotic method (Plaszczynski et al. 2014). *Left:* Extinction. *Right:* Submillimetre emission. Note which variables have the largest errors: in the optical, τ_V (x axis), in the submillimetre, P_S (y axis). In the left panel, the line (blue) represents the “classical” upper envelope, $p_V = 0.0315 \tau_V$ (Serkowski et al. 1975). This upper envelope has been transferred to the right panel using the derived value for $R_{S/V}$.

as the ratio between the polarization efficiencies in the submillimetre and the optical, is

$$R_{S/V} = (P_S/I_S)/(p_V/\tau_V) = 4.3 \pm 0.2 \text{ (stat.)} \pm 0.4 \text{ (syst.)}, \quad (20)$$

where the statistical uncertainty is from the bootstrap analysis and many consistency checks (Sect. 6.2) and the systematic error is dominated by our incomplete knowledge of the small correction of *Planck* data for leakage of intensity into polarization (Sect. 3.1).

We cannot conclude that $R_{S/V}$ is uniform throughout the local diffuse ISM, although this might be the case. We have found some evidence for mild variations of $R_{S/V}$ from region to region, as well as with T_{dust} . Such variations might be as large as ± 0.5 in $R_{S/V}$. However, the evidence is still unclear, because of the statistical uncertainties in the analysis and because of the lack of precision in the March 2013 data regarding the correction of the small leakage of intensity into polarization (Sect. 3.1).²³ Needless to say, for individual lines of sight, actual departures from the mean $R_{S/V}$ could still be significant.

Similarly we found the ratio between the polarized intensity in the submillimetre and the degree of polarization in the optical:

$$R_{P/p} = P_S/p_V = [5.6 \pm 0.2 \text{ (stat.)} \pm 0.4 \text{ (syst.)}] \text{ MJy sr}^{-1}. \quad (21)$$

This analysis of the March 2013 *Planck* data suggests that the measured $R_{S/V}$ is compatible with a range of dust models, not yet very discriminating among them. By contrast, the measured $R_{P/p}$ is higher than model predictions by a factor of about 2.5. Thus, the simpler polarization ratio $R_{P/p}$ turns out to provide a more stringent constraint on dust models than $R_{S/V}$. Future dust models are needed that will satisfy the constraints provided by both $R_{S/V}$ and $R_{P/p}$, as well as by the spectral dependencies in the optical and submillimetre. Understanding the polarized intensity

from thermal dust will be important in refining the separation of this contamination of the CMB.

Acknowledgements. The development of *Planck* has been supported by: ESA; CNES and CNRS/INSU-IN2P3-INP (France); ASI, CNR, and INAF (Italy); NASA and DoE (USA); STFC and UKSA (UK); CSIC, MICINN, JA and RES (Spain); Tekes, Aof and CSC (Finland); DLR and MPG (Germany); CSA (Canada); DTU Space (Denmark); SER/SSO (Switzerland); RCN (Norway); SFI (Ireland); FCT/MCTES (Portugal); and PRACE (EU). A description of the Planck Collaboration and a list of its members, including the technical or scientific activities in which they have been involved, can be found at http://www.sciops.esa.int/index.php?project=planck&page=Planck_Collaboration. The research leading to these results has received funding from the European Research Council under the European Union’s Seventh Framework Programme (FP7/2007-2013) / ERC grant agreement no. 267934. This research has made use of the SIMBAD database and the VizieR catalogue access tool, operated at CDS, Strasbourg, France, and NASA’s Astrophysics Data System Service.

References

- Ade, P. A. R., Savini, G., Sudiwala, R., et al. 2010, *A&A*, 520, A11
- Andersson, B.-G. & Potter, S. B. 2007, *The Astrophysical Journal*, 665, 369
- Benoît, A., Ade, P. A. R., Amblard, A., et al. 2004, *Astronomy and Astrophysics*, 424, 571
- Binney, J. & Merrifield, M. 1998, *Galactic astronomy* / James Binney and Michael Merrifield. Princeton
- Bohlin, R. C., Savage, B. D., & Drake, J. F. 1978, *ApJ*, 224, 132
- Bohlin, R. C., Savage, B. D., & Drake, J. F. 1978, *The Astrophysical Journal*, 224, 132
- Cecchi-Pestellini, C., Cacciola, A., Iatì, M. A., et al. 2010, *Monthly Notices of the Royal Astronomical Society*, 1053
- Chiar, J. E., Adamson, A. J., Whittet, D. C. B., et al. 2006, *The Astrophysical Journal*, 651, 268
- Compiegne, M., Verstraete, L., Jones, A., et al. 2011, *Astronomy and Astrophysics*, 525, 103
- Compiegne, M., Verstraete, L., Jones, A., et al. 2011, *A&A*, 525, A103
- Davis, L. & Greenstein, J. L. 1951, *Astrophysical Journal*, 114, 206
- Draine, B. T. & Fraisse, A. A. 2009, *ApJ*, 696, 1
- Draine, B. T. & Hensley, B. 2013, *The Astrophysical Journal*, 765, 159
- Draine, B. T. & Li, A. 2007, *The Astrophysical Journal*, 657, 810
- Efron, B. & Tibshirani, R. J. 1993, *An Introduction to the Bootstrap* (New York, NY: Chapman & Hall)
- Fitzgerald, M. P. 1970, *Astronomy and Astrophysics*, 4, 234
- Fitzpatrick, E. L. 2004, *Astrophysics of Dust*, 309, 33

²³ Our data analysis on the latest version of the maps available to the consortium show much smaller effects of leakage and the results are consistent within the uncertainties quoted in this paper; there is little evidence for regional variations or variations with T_{dust} .

Fitzpatrick, E. L. & Massa, D. 2007, *The Astrophysical Journal*, 663, 320

Gorski, K. M., Hivon, E., Banday, A. J., et al. 2005, *The Astrophysical Journal*, 622, 759

Gray, D. F. 1992, *Camb. Astrophys. Ser.*

Hall, J. S. 1949, *Science*, 109, 166

Heiles, C. 2000, *The Astronomical Journal*, 119, 923

Hildebrand, R. H., Dotson, J. L., Dowell, C. D., Schleuning, D. A., & Vaillancourt, J. E. 1999, *The Astrophysical Journal*, 516, 834

Hiltner, W. A. 1949, *Nature*, 163, 283

Hoang, T., Lazarian, A., & Martin, P. G. 2013, *The Astrophysical Journal*, 779, 152

Johnson, H. L. 1966, *Annual Review of Astronomy and Astrophysics*, 4, 193

Jones, A. P., Fanciullo, L., Köhler, M., et al. 2013, *Astronomy and Astrophysics*, 558, 62

Kalberla, P. M. W., Burton, W. B., Hartmann, D., et al. 2005, *Astronomy and Astrophysics*, 440, 775

Kharchenko, N. V. & Roeser, S. 2009, *VizieR On-line Data Catalog*, 1280, 0

Lamarre, J., Puget, J., Ade, P. A. R., et al. 2010, *A&A*, 520, A9

Lang, K. R. 1992, *Astrophysical Data I. Planets and Stars*

Lee, H. M. & Draine, B. T. 1985, *Astrophysical Journal*, 290, 211

Li, A. & Draine, B. T. 2001, *ApJ*, 554, 778

Li, A. & Greenberg, J. M. 1997, *Astronomy and Astrophysics*, 323, 566

Martin, P. G. 2007, *EAS Publications Series*, 23, 165

Martin, P. G., Adamson, A. J., Whittet, D. C. B., et al. 1992, *Astrophysical Journal*, 392, 691

Martin, P. G., Clayton, G. C., & Wolff, M. J. 1999, *The Astrophysical Journal*, 510, 905

Martin, P. G., Roy, A., Bontemps, S., et al. 2012, *ApJ*, 751, 28

Mathewson, D. S., Ford, V. I., Krautter, J., & Outred, M. 1978, *Bull. Inf. Cent. Données Stellaires*, 14, 115

Mathewson, D. S. & Ford, V. L. 1971, *Monthly Notices of the Royal Astronomical Society*, 153, 525

Naghizadeh-Khouei, J. & Clarke, D. 1993, *Astronomy and Astrophysics*, 274, 968

Planck Collaboration XXIV. 2011, *A&A*, 536, A24

Planck Collaboration I. 2014, *A&A*, in press

Planck Collaboration VI. 2014, *A&A*, in press

Planck Collaboration VII. 2014, *A&A*, in press

Planck Collaboration VIII. 2014, *A&A*, in press

Planck Collaboration IX. 2014, *A&A*, in press

Planck Collaboration X. 2014, *A&A*, in press

Planck Collaboration XI. 2014, *A&A*, in press

Planck Collaboration XII. 2014, *A&A*, in press

Planck Collaboration XIII. 2014, *A&A*, in press

Planck Collaboration XIV. 2014, *A&A*, in press

Planck Collaboration XVI. 2014, *A&A*, in press

Planck Collaboration XXX. 2014, *A&A*, in press

Planck Collaboration Int. XVII. 2014, *A&A*, in press

Planck Collaboration Int. XIX. 2014, *A&A*, submitted, [arXiv:astro-ph/1405.xxxx]

Planck Collaboration Int. XX. 2014, *A&A*, submitted, [arXiv:astro-ph/1405.xxxx]

Planck Collaboration Int. XXII. 2014, *A&A*, submitted, [arXiv:astro-ph/1405.xxxx]

Planck Collaboration Int. XXV. 2014, *A&A*, to be submitted, [arXiv:astro-ph/14xx.xxxx]

Plazczynski, S., Montier, L., Levrier, F., & Tristram, M. 2014, *MNRAS*, 439, 4048

Quinn, J. L. 2012, *Astronomy and Astrophysics*, 538, 65

Roy, A., Martin, P. G., Polychroni, D., et al. 2013, *ApJ*, 763, 55

Savage, B. D., Massa, D., Meade, M., & Wesselius, P. R. 1985, *Astrophysical Journal Supplement Series* (ISSN 0067-0049), 59, 397

Serkowski, K. 1958, *Acta Astron.*, 8, 135

Serkowski, K., Mathewson, D. S., & Ford, V. L. 1975, *Astrophysical Journal*, 196, 261

Siebmorgen, R., Voshchinnikov, N. V., & Bagnulo, S. 2013, *arXiv.org*, 3148

Simmons, J. F. L. & Stewart, B. G. 1985, *Astronomy and Astrophysics* (ISSN 0004-6361), 142, 100

Skrutskie, M. F., Cutri, R. M., Stiening, R., et al. 2006, *AJ*, 131, 1163

Stein, W. 1966, *ApJ*, 144, 318

Taylor, M. B. 2005, in *Astronomical Society of the Pacific Conference Series*, Vol. 347, *Astronomical Data Analysis Software and Systems XIV*, ed. P. Shopbell, M. Britton, & R. Ebert, 29

Valencic, L. A., Clayton, G. C., & Gordon, K. D. 2004, *The Astrophysical Journal*, 616, 912

Voshchinnikov, N. V. 2012, *Journal of Quantitative Spectroscopy and Radiative Transfer*, 113, 2334

Wardle, J. F. C. & Kronberg, P. P. 1974, *ApJ*, 194, 249

Wegner, W. 2002, *Baltic Astronomy*, 11, 1

Wegner, W. 2003, *VizieR On-line Data Catalog*, 0010, 32401

Appendix A: Uncertainties for polarization quantities

We start with the values of the Stokes parameters, I , Q , and U , and the noise covariance matrix, $[C]$, at the position of each star. By definition, the uncertainties σ_{Q_S} of Q_S and σ_{U_S} of U_S are calculated from the variances $\sigma_{Q_S}^2 \equiv C_{QQ}$ and $\sigma_{U_S}^2 \equiv C_{UU}$, respectively.

The variance of the polarized intensity $P_S \equiv \sqrt{Q_S^2 + U_S^2}$ (without bias correction) is

$$\begin{aligned} \sigma_{P_S}^2 &= \left\langle \left(\frac{\partial P}{\partial Q} \delta Q + \frac{\partial P}{\partial U} \delta U \right)^2 \right\rangle \\ &= \frac{Q_S^2 C_{QQ} + U_S^2 C_{UU} + 2 Q_S U_S C_{QU}}{P_S^2}, \end{aligned} \quad (\text{A.1})$$

from which we derive the S/N of the polarization intensity, P/σ_P . For the uncertainty in the position angle ψ_S we use the approximate formula in Eq. 6, which is appropriate because we always require the S/N to be larger than 3.²⁴

The uncertainty of the projected polarization fraction Q_S/I_S has the following dependence:

$$\delta\left(\frac{Q}{I}\right) = \frac{\partial(Q/I)}{\partial Q} \delta Q + \frac{\partial(Q/I)}{\partial I} \delta I = \frac{1}{I} \delta Q - \frac{Q}{I^2} \delta I, \quad (\text{A.2})$$

and the same holds for U_S/I_S . The covariance of Q_S/I_S with U_S/I_S follows:

$$\begin{aligned} C_{Q/I, U/I} &= \left\langle \delta\left(\frac{Q}{I}\right) \delta\left(\frac{U}{I}\right) \right\rangle \\ &= \left\langle \frac{1}{I^2} \delta Q \delta U + \frac{QU}{I^4} \delta I^2 - \frac{U}{I^3} \delta I \delta Q - \frac{Q}{I^3} \delta I \delta U \right\rangle \\ &= \frac{I_S^2 C_{QU} + Q_S U_S C_{II} - I_S Q_S C_{IU} - I_S U_S C_{IQ}}{I_S^4}. \end{aligned} \quad (\text{A.3})$$

The uncertainties σ_{Q_S/I_S} and σ_{U_S/I_S} , used for plotting only, are derived simply from the variances $C_{Q/I, Q/I}$ and $C_{U/I, U/I}$.

When the data are smoothed, with the method described in Appendix A of Planck Collaboration Int. XIX (2014),²⁵ the formulae hold substituting the smoothed Stokes parameters and the elements of the corresponding covariance matrix, $[C]$.

Appendix B: Deriving $E(B - V)$ from the Kharchenko & Roeser star catalogue

The Kharchenko & Roeser (2009) catalogue (SIMBAD reference code I/280 B) used for the derivation of $E(B - V)$ is a compilation of space and ground-based observational data for more than 2.5 million stars. The catalogued data include, among others, B and V magnitudes in the Johnson system, K magnitude, HD number, and the spectral type and luminosity class of the

²⁴ The uncertainties in P_S and ψ_S are used just for the selection process and for plotting, not for the fitting, which involves the full noise covariance matrix; see Sect. 6.1.

²⁵ The coordinates of the central pixel, J , of the smoothing beam are replaced by those of the star.

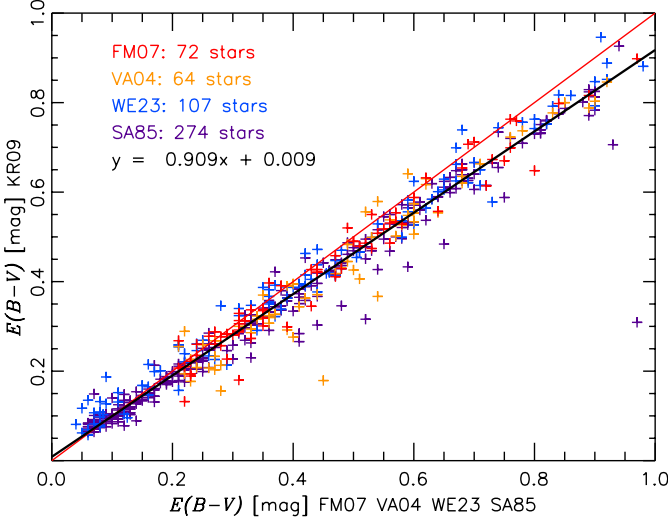


Fig. B.1. Correlation between our derived $E(B - V)$ from the Kharchenko & Roeser (2009) catalogue with that for common stars in the FM07, VA04, and WE23 samples. Only data with S/N on $E(B - V)$ larger than 3 are presented. The red line is a 1:1 correlation, while the black line is a fit.

star. TOPCAT²⁶ (Taylor 2005) was used to cross-match the polarization (Heiles 2000) and extinction (Kharchenko & Roeser 2009) catalogues with the HD number as the first-order criterion. Where two or more stars are identified with the same number, the one for which the visual magnitude is closest to that in the polarization catalogue was retained. For the rest of the catalogue, a coordinate-match criterion with a $2'$ radius was applied, using the visual magnitude to choose between candidates if necessary.

A table of intrinsic colours $(B - V)_0$ for different spectral classifications was compiled using data from Johnson (1966), Fitzgerald (1970), Lang (1992), Gray (1992), and Binney & Merrifield (1998). The colour excess for each of star was calculated according to $E(B - V) = (B - V)_{\text{KR09}} - (B - V)_0$, using the B and V magnitudes and the corresponding intrinsic colour deduced from the spectral classification in the Kharchenko & Roeser (2009) catalogue. Following Savage et al. (1985), Be stars and stars with spectral types B8 and B9 were removed.

Figure B.1 presents, as a control check, the good correlation we obtain when comparing our derived $E(B - V)$ with that of the FM07, VA04, and WE23 samples, for stars in common. However, compared to other samples, our KR09 $E(B - V)$ tends to underestimate the reddening to the star by about 9%. This potential discrepancy has only a small impact on the derived $R_{S/V}$ (the KR09 sample represents one third of our sample, see Table 1) and does not affect $R_{P/P}$.

¹ APC, AstroParticule et Cosmologie, Université Paris Diderot, CNRS/IN2P3, CEA/Irfu, Observatoire de Paris, Sorbonne Paris Cité, 10, rue Alice Domon et Léonie Duquet, 75205 Paris Cedex 13, France

² Aalto University Metsähovi Radio Observatory and Dept of Radio Science and Engineering, P.O. Box 13000, FI-00076 AALTO, Finland

³ African Institute for Mathematical Sciences, 6-8 Melrose Road, Muizenberg, Cape Town, South Africa

⁴ Agenzia Spaziale Italiana Science Data Center, Via del Politecnico snc, 00133, Roma, Italy

- ⁵ Agenzia Spaziale Italiana, Viale Liegi 26, Roma, Italy
- ⁶ Astrophysics Group, Cavendish Laboratory, University of Cambridge, J J Thomson Avenue, Cambridge CB3 0HE, U.K.
- ⁷ Astrophysics & Cosmology Research Unit, School of Mathematics, Statistics & Computer Science, University of KwaZulu-Natal, Westville Campus, Private Bag X54001, Durban 4000, South Africa
- ⁸ Atacama Large Millimeter/submillimeter Array, ALMA Santiago Central Offices, Alonso de Cordova 3107, Vitacura, Casilla 763 0355, Santiago, Chile
- ⁹ CITA, University of Toronto, 60 St. George St., Toronto, ON M5S 3H8, Canada
- ¹⁰ CNRS, IRAP, 9 Av. colonel Roche, BP 44346, F-31028 Toulouse cedex 4, France
- ¹¹ California Institute of Technology, Pasadena, California, U.S.A.
- ¹² Centro de Estudios de Física del Cosmos de Aragón (CEFCA), Plaza San Juan, 1, planta 2, E-44001, Teruel, Spain
- ¹³ Computational Cosmology Center, Lawrence Berkeley National Laboratory, Berkeley, California, U.S.A.
- ¹⁴ Consejo Superior de Investigaciones Científicas (CSIC), Madrid, Spain
- ¹⁵ DSM/Irfu/SPP, CEA-Saclay, F-91191 Gif-sur-Yvette Cedex, France
- ¹⁶ DTU Space, National Space Institute, Technical University of Denmark, Elektrovej 327, DK-2800 Kgs. Lyngby, Denmark
- ¹⁷ Département de Physique Théorique, Université de Genève, 24, Quai E. Ansermet, 1211 Genève 4, Switzerland
- ¹⁸ Departamento de Física Fundamental, Facultad de Ciencias, Universidad de Salamanca, 37008 Salamanca, Spain
- ¹⁹ Departamento de Física, Universidad de Oviedo, Avda. Calvo Sotelo s/n, Oviedo, Spain
- ²⁰ Department of Astronomy and Astrophysics, University of Toronto, 50 Saint George Street, Toronto, Ontario, Canada
- ²¹ Department of Astrophysics/IMAPP, Radboud University Nijmegen, P.O. Box 9010, 6500 GL Nijmegen, The Netherlands
- ²² Department of Electrical Engineering and Computer Sciences, University of California, Berkeley, California, U.S.A.
- ²³ Department of Physics and Astronomy, Dana and David Dornsife College of Letter, Arts and Sciences, University of Southern California, Los Angeles, CA 90089, U.S.A.
- ²⁴ Department of Physics and Astronomy, University College London, London WC1E 6BT, U.K.
- ²⁵ Department of Physics, Florida State University, Keen Physics Building, 77 Chieftan Way, Tallahassee, Florida, U.S.A.
- ²⁶ Department of Physics, Gustaf Hållströmin katu 2a, University of Helsinki, Helsinki, Finland
- ²⁷ Department of Physics, Princeton University, Princeton, New Jersey, U.S.A.
- ²⁸ Department of Physics, University of California, Santa Barbara, California, U.S.A.
- ²⁹ Department of Physics, University of Illinois at Urbana-Champaign, 1110 West Green Street, Urbana, Illinois, U.S.A.
- ³⁰ Dipartimento di Fisica e Astronomia G. Galilei, Università degli Studi di Padova, via Marzolo 8, 35131 Padova, Italy
- ³¹ Dipartimento di Fisica e Scienze della Terra, Università di Ferrara, Via Saragat 1, 44122 Ferrara, Italy
- ³² Dipartimento di Fisica, Università La Sapienza, P. le A. Moro 2, Roma, Italy
- ³³ Dipartimento di Fisica, Università degli Studi di Milano, Via Celoria, 16, Milano, Italy
- ³⁴ Dipartimento di Fisica, Università degli Studi di Trieste, via A. Valerio 2, Trieste, Italy
- ³⁵ Dipartimento di Fisica, Università di Roma Tor Vergata, Via della Ricerca Scientifica, 1, Roma, Italy
- ³⁶ Discovery Center, Niels Bohr Institute, Blegdamsvej 17, Copenhagen, Denmark
- ³⁷ Dpto. Astrofísica, Universidad de La Laguna (ULL), E-38206 La Laguna, Tenerife, Spain

²⁶ <http://www.starlink.ac.uk/topcat/>

- ³⁸ European Southern Observatory, ESO Vitacura, Alonso de Cordova 3107, Vitacura, Casilla 19001, Santiago, Chile
- ³⁹ European Space Agency, ESAC, Planck Science Office, Camino bajo del Castillo, s/n, Urbanización Villafranca del Castillo, Villanueva de la Cañada, Madrid, Spain
- ⁴⁰ European Space Agency, ESTEC, Keplerlaan 1, 2201 AZ Noordwijk, The Netherlands
- ⁴¹ Helsinki Institute of Physics, Gustaf Hållströmin katu 2, University of Helsinki, Helsinki, Finland
- ⁴² INAF - Osservatorio Astrofisico di Catania, Via S. Sofia 78, Catania, Italy
- ⁴³ INAF - Osservatorio Astronomico di Padova, Vicolo dell'Osservatorio 5, Padova, Italy
- ⁴⁴ INAF - Osservatorio Astronomico di Roma, via di Frascati 33, Monte Porzio Catone, Italy
- ⁴⁵ INAF - Osservatorio Astronomico di Trieste, Via G.B. Tiepolo 11, Trieste, Italy
- ⁴⁶ INAF/IASF Bologna, Via Gobetti 101, Bologna, Italy
- ⁴⁷ INAF/IASF Milano, Via E. Bassini 15, Milano, Italy
- ⁴⁸ INFN, Sezione di Bologna, Via Irnerio 46, I-40126, Bologna, Italy
- ⁴⁹ INFN, Sezione di Roma 1, Università di Roma Sapienza, Piazzale Aldo Moro 2, 00185, Roma, Italy
- ⁵⁰ INFN/National Institute for Nuclear Physics, Via Valerio 2, I-34127 Trieste, Italy
- ⁵¹ IPAG: Institut de Planétologie et d'Astrophysique de Grenoble, Université Joseph Fourier, Grenoble 1 / CNRS-INSU, UMR 5274, Grenoble, F-38041, France
- ⁵² Imperial College London, Astrophysics group, Blackett Laboratory, Prince Consort Road, London, SW7 2AZ, U.K.
- ⁵³ Infrared Processing and Analysis Center, California Institute of Technology, Pasadena, CA 91125, U.S.A.
- ⁵⁴ Institut d'Astrophysique Spatiale, CNRS (UMR8617) Université Paris-Sud 11, Bâtiment 121, Orsay, France
- ⁵⁵ Institut d'Astrophysique de Paris, CNRS (UMR7095), 98 bis Boulevard Arago, F-75014, Paris, France
- ⁵⁶ Institute for Space Sciences, Bucharest-Magurale, Romania
- ⁵⁷ Institute of Astronomy, University of Cambridge, Madingley Road, Cambridge CB3 0HA, U.K.
- ⁵⁸ Institute of Theoretical Astrophysics, University of Oslo, Blindern, Oslo, Norway
- ⁵⁹ Instituto de Astrofísica de Canarias, C/Vía Láctea s/n, La Laguna, Tenerife, Spain
- ⁶⁰ Instituto de Astronomia, Geofísica e Ciências Atmosféricas, Universidade de São Paulo, São Paulo, SP 05508-090, Brazil
- ⁶¹ Instituto de Física de Cantabria (CSIC-Universidad de Cantabria), Avda. de los Castros s/n, Santander, Spain
- ⁶² Jet Propulsion Laboratory, California Institute of Technology, 4800 Oak Grove Drive, Pasadena, California, U.S.A.
- ⁶³ Jodrell Bank Centre for Astrophysics, Alan Turing Building, School of Physics and Astronomy, The University of Manchester, Oxford Road, Manchester, M13 9PL, U.K.
- ⁶⁴ Kavli Institute for Cosmology Cambridge, Madingley Road, Cambridge, CB3 0HA, U.K.
- ⁶⁵ LAL, Université Paris-Sud, CNRS/IN2P3, Orsay, France
- ⁶⁶ LERMA, CNRS, Observatoire de Paris, 61 Avenue de l'Observatoire, Paris, France
- ⁶⁷ Laboratoire AIM, IRFU/Service d'Astrophysique - CEA/DSM - CNRS - Université Paris Diderot, Bât. 709, CEA-Saclay, F-91191 Gif-sur-Yvette Cedex, France
- ⁶⁸ Laboratoire Traitement et Communication de l'Information, CNRS (UMR 5141) and Télécom ParisTech, 46 rue Barrault F-75634 Paris Cedex 13, France
- ⁶⁹ Laboratoire de Physique Subatomique et de Cosmologie, Université Joseph Fourier Grenoble I, CNRS/IN2P3, Institut National Polytechnique de Grenoble, 53 rue des Martyrs, 38026 Grenoble cedex, France
- ⁷⁰ Laboratoire de Physique Théorique, Université Paris-Sud 11 & CNRS, Bâtiment 210, 91405 Orsay, France
- ⁷¹ Lawrence Berkeley National Laboratory, Berkeley, California, U.S.A.
- ⁷² Max-Planck-Institut für Astrophysik, Karl-Schwarzschild-Str. 1, 85741 Garching, Germany
- ⁷³ National University of Ireland, Department of Experimental Physics, Maynooth, Co. Kildare, Ireland
- ⁷⁴ Niels Bohr Institute, Blegdamsvej 17, Copenhagen, Denmark
- ⁷⁵ Observational Cosmology, Mail Stop 367-17, California Institute of Technology, Pasadena, CA, 91125, U.S.A.
- ⁷⁶ Optical Science Laboratory, University College London, Gower Street, London, U.K.
- ⁷⁷ SISSA, Astrophysics Sector, via Bonomea 265, 34136, Trieste, Italy
- ⁷⁸ School of Physics and Astronomy, Cardiff University, Queens Buildings, The Parade, Cardiff, CF24 3AA, U.K.
- ⁷⁹ Space Sciences Laboratory, University of California, Berkeley, California, U.S.A.
- ⁸⁰ Special Astrophysical Observatory, Russian Academy of Sciences, Nizhnij Arkhyz, Zelenchukskiy region, Karachai-Cherkessian Republic, 369167, Russia
- ⁸¹ Sub-Department of Astrophysics, University of Oxford, Keble Road, Oxford OX1 3RH, U.K.
- ⁸² UPMC Univ Paris 06, UMR7095, 98 bis Boulevard Arago, F-75014, Paris, France
- ⁸³ Université de Toulouse, UPS-OMP, IRAP, F-31028 Toulouse cedex 4, France
- ⁸⁴ Universities Space Research Association, Stratospheric Observatory for Infrared Astronomy, MS 232-11, Moffett Field, CA 94035, U.S.A.
- ⁸⁵ University of Granada, Departamento de Física Teórica y del Cosmos, Facultad de Ciencias, Granada, Spain
- ⁸⁶ Warsaw University Observatory, Aleje Ujazdowskie 4, 00-478 Warszawa, Poland